HHS Public Access

Author manuscript

Nat Metab. Author manuscript; available in PMC 2023 August 26.

Published in final edited form as:

Nat Metab. 2023 February ; 5(2): 207–218. doi:10.1038/s42255-022-00728-0.

Phagocytosis in the retina promotes local insulin production in the eye

J. Iker Etchegaray[1,2,3], **Shannon Kelley**[1,2,3], **Kristen Penberthy**[1,2], **Laura Karvelyte**[1,2,3], **Yosuke Nagasaka**[4], **Sofia Gasperino**[1,2,3], **Soumen Paul**[5], **Vikram Seshadri**[5], **Michael Raymond**[1,2], **Ana Royo Marco**[2], **Jonathan Pinney**[1,2], **Marta Stremska**[2,3], **Brady Barron**[1,2,3], **Christopher Lucas**[1,2,6], **Nishikant Wase**[7], **Yong Fan**[8], **Emil Unanue**[3], **Bijoy Kundu**[5], **Tal Burstyn-Cohen**[9], **Justin Perry**[10], **Jayakrishna Ambati**[4,11], **Kodi S. Ravichandran**[1,2,9,12,✉]

[1]Center for Cell Clearance, University of Virginia, Charlottesville, VA, USA

[2]Department of Microbiology, Immunology, and Cancer Biology, University of Virginia, Charlottesville, VA, USA

[3]Department of Pathology and Immunology, Washington University School of Medicine, St. Louis, MO, USA

[4]Center for Advanced Vision Science, University of Virginia, Charlottesville, VA, USA

[5]Department of Radiology and Medical Imaging, University of Virginia, Charlottesville, VA, USA

[6]University of Edinburgh, Edinburgh, UK

[7]Biomolecular Analysis Facility, University of Virginia, Charlottesville, VA, USA

[8]Drexel University, Philadelphia, PA, USA

[9]Hadassah Medical School, Hebrew University of Jerusalem, Jerusalem, Israel

[10]Memorial Sloan Kettering Cancer Center, New York, NY, USA

[11]Ophthalmology, University of Virginia, Charlottesville, VA, USA

✉**Correspondence and requests for materials** should be addressed to Kodi S. Ravichandran, kodi@wustl.edu.

Author contributions

J.I.E. and K.S.R. designed all experiments and wrote and composed the manuscript. J.I.E. performed most of the experiments. S.K. performed all immunoblots. K.P. performed RNA-seq of MerTK KO mice. L.K. assisted with eye dissections. Y.N. and J.A. conducted ERG experiments. S.G. provided input and generated figures. S.P., V.S. and B.K. carried out PET experiments. M.R., C.L. and E.U. provided conceptual advice and/or helped with specific experiments. A.R.M. helped with the RPE phagocytosis assay. J. Pinney analyzed RNA-seq data and mined public datasets. M.S. assisted with ELISAs. B.B. performed glucose tolerance assays. N.W. performed metabolomics. Y.F. provided *Ins2*$^{f/f}$ mice. T.B.-C. conducted mouse insulin immunofluorescence assays. J. Perry analyzed metabolomics data and gave conceptual advice.

Competing interests

The authors declare no competing interests.

Additional information

Extended data is available for this paper at https://doi.org/10.1038/s42255-022-00728-0.

Supplementary information The online version contains supplementary material available at https://doi.org/10.1038/s42255-022-00728-0.

Peer review information *Nature Metabolism* thanks the anonymous reviewers for their contribution to the peer review of this work. Primary Handling Editor: Christoph Schmitt in collaboration with the *Nature Metabolism* team.

[12]VIB/UGent Inflammation Research Centre, and Biomedical Molecular Biology, Ghent University, Ghent, Belgium

Abstract

The retina is highly metabolically active, relying on glucose uptake and aerobic glycolysis. Situated in close contact to photoreceptors, a key function of cells in the retinal pigment epithelium (RPE) is phagocytosis of damaged photoreceptor outer segments (POS). Here we identify RPE as a local source of insulin in the eye that is stimulated by POS phagocytosis. We show that *Ins2* messenger RNA and insulin protein are produced by RPE cells and that this production correlates with RPE phagocytosis of POS. Genetic deletion of phagocytic receptors ('loss of function') reduces *Ins2*, whereas increasing the levels of the phagocytic receptor MerTK ('gain of function') increases *Ins2* production in male mice. Contrary to pancreas-derived systemic insulin, RPE-derived local insulin is stimulated during starvation, which also increases RPE phagocytosis. Global or RPE-specific *Ins2* gene deletion decreases retinal glucose uptake in starved male mice, dysregulates retinal physiology, causes defects in phototransduction and exacerbates photoreceptor loss in a mouse model of retinitis pigmentosa. Collectively, these data identify RPE cells as a phagocytosis-induced local source of insulin in the retina, with the potential to influence retinal physiology and disease.

In the retina, a group of RPE cells reside in close apposition to the photoreceptors to form the outer blood–retinal barrier. The RPE critically contributes to photoreceptor metabolic homeostasis in multiple ways; taking up glucose from circulation and passing it to photoreceptors, and to allow glucose 'pass-through', RPE cells express GLUT1, a glucose transporter, on both basolateral and apical membranes[1,2]. Photoreceptors are highly metabolically active and glucose is almost entirely metabolized through aerobic glycolysis[3]. RPE cells also have a specialized metabolism that utilizes lactate, the by-product of aerobic glycolysis by the photoreceptors[2]. Lack of proper glucose uptake by the retina can impair vision and contribute to diseases such as retinitis pigmentosa[4–6].

RPE performs another critical function in retinal physiology: phagocytosis of photoreceptors that undergo damage during the day due to light. The RPE uptake of POS is circadian regulated and starts around dawn/light onset[7]. The ingested POS also fuel RPE and retina metabolism[8,9]. Mer tyrosine kinase (MerTK)-dependent POS phagocytosis not only spares glucose from being consumed by the RPE[8], but upregulates GLUT1 (ref. [9]) to allow more glucose to be taken up from circulation into the retina; however, the mechanisms by which POS phagocytosis modulates retina metabolism directly are still poorly understood.

Insulin is a peptide hormone produced by the pancreas upon feeding and promotes uptake of glucose (and other metabolic substrates) by tissues. Although lack of pancreatic insulin contributes to diseases of the retina[10] the role of circulating insulin on signaling within the retina is less clear. Indeed, multiple lines of research have shown the retina to be 'insensitive' to systemic insulin; injection of insulin into the portal vein of rats leads to insulin receptor (InsR) phosphorylation in muscle but not in the retina[11]. Radioactively labeled insulin (injected directly into the cilioretinal artery of cows) does not cross into the retina[12] and insulin protein levels and InsR phosphorylation in the retina of rats does not

change, regardless of whether the animal has been fed or fasted[11,13]. Additionally, ablating pancreatic insulin does not change retinal insulin protein levels and instead, leads to an increase in glucose levels within the eye[14]. Paradoxically, however, research has shown that InsR signaling in the retina is crucial to homeostasis[15].

Here, we discover phagocytosis by the RPE as a trigger for local insulin generation in the retina, especially under conditions of nutrient scarcity/starvation when systemic insulin is low and this RPE-derived insulin promotes retinal glucose uptake and retinal homeostasis.

RPE as a source of insulin in the eye

MerTK is a key tyrosine kinase receptor, expressed by the RPE, involved in phagocytosis of photoreceptors and retinal homeostasis[16,17]. Previously, we observed transgenic expression of another phagocytic receptor (BAI1) cannot rescue retinal degeneration in MerTK knockout (KO) mice[18], in part due to unique gene signatures induced by MerTK. Re-analyzing the RNA-seq dataset[18], we noted that one of the down-regulated genes in RPE from MerTK knockout mice was *Ins2*, which encodes insulin (Fig. 1a). Mice have two insulin-encoding genes *Ins1* and *Ins2*, both expressed in the pancreas[19]. In our RPE RNAseq dataset, *Ins1* was undetectable in wild-type (WT) and MerTK KO mice. We did not detect altered expression of other factors linked to growth and metabolism, such as insulin-like growth factor-1, insulin-like growth factor-2, transforming growth factor (TGF)-β1, TGF-β2 or TGF-β3, vascular endothelial growth factor or fibroblast growth factor (Fig. 1a). Comparing *Ins2* expression among different tissues, the eye had the second highest expression after the pancreas (Fig. 1b and Extended Data Fig. 1a). The thymus expresses *Ins2* as part of establishing T-cell tolerance to insulin[20] and thymic *Ins2* levels were lower than the eye.

When we compared *Ins2* expression in purified RPE versus the whole retina, *Ins2* was predominantly expressed in the RPE (Fig. 1c). Notably, expression of *Ins2* was detectable in purified and cultured primary RPE ex vivo (devoid of other cell types); in contrast, *Ins2* was undetectable in mouse embryonic fibroblasts (Fig. 1d). Further, in situ hybridization (RNAScope) showed *Ins2* expression primarily in the RPE with little expression in the rest of retina (Fig. 1e).

To further confirm RPE expression of *Ins2*, we crossed YFP-reporter mice to *Best1*-Cre mice (where the Cre recombinase is expressed under the *Bestrophin1* promoter). As *Best1*-Cre expression is not 100% penetrant within the RPE population[1,21], we purified YFP-expressing RPE cells via flow cytometry, isolated their nuclei and performed PCR with reverse transcription (RT–PCR) (Extended Data Fig. 1b)[21]. *Ins2* expression was readily detected in the purified RPE nuclei, comparable to *MerTK* (Fig. 1f). In the same conditions, *rhodopsin*, a photoreceptor-specific gene[18], was undetectable (Fig. 1f). Further, purified RPE only expressed *Ins2* (not *Ins1*) (Fig. 1c).

To genetically ablate *Ins2* gene expression in the RPE, we crossed mice carrying floxed *Ins2* alleles ($Ins^{2f/f}$) with *Best1*-Cre. Despite *Best1*-Cre expression in the RPE being not fully penetrant (refs. [1,21] and Extended Data Fig. 1b), RPE from *Best1*-Cre $Ins^{2f/f}$ mice

had decreased *Ins2* mRNA (Fig. 1g). As control, we crossed $Ins^{2f/f}$ mice to *rhodopsin* promoter driven-Cre (*Rhod*-Cre), targeting the photoreceptors. RPE from *Rhod*-Cre $Ins^{2f/f}$ mice did not show a decrease in *Ins2* (Extended Data Fig. 1c), confirming RPE-specific *Ins2* expression.

At the protein level, insulin was detected by ELISA using protein extracts from purified RPE (Fig. 1h); further, immunofluorescence on retinal sections revealed insulin protein within the RPE (Fig. 1h). To assess insulin secretion by the RPE, we measured C-peptide 2, a by-product of proinsulin processing that gets co-released with insulin and is used as a common metric for insulin release[22]. Supernatants of isolated eye cups ex vivo contained C-peptide 2 (Fig. 1i). Further, treatment with potassium chloride (KCl), an inducer of pancreatic insulin release, enhanced C-peptide 2 levels in the eye cup supernatants (Fig. 1i). These data revealed that RPE can produce and release insulin.

We also examined insulin expression in the RPE of primates via different approaches. Mining an existing macaque retinal single-cell RNA-seq data indicated *Ins* mRNA in the RPE and RPE 'like' cells[23] (Extended Data Fig. 2). Further, insulin expression was detectable in the RPE of human retinal sections (Fig. 1j). C-peptide was also detected in the human retina (Extended Data Fig. 1d). These multiple orthogonal pieces of data demonstrated RPE as a source of *Ins2* mRNA and insulin protein in the eye.

RPE insulin is regulated differently from systemic insulin

While pancreatic insulin release is induced by feeding, both *Ins1* and *Ins2* transcript levels plummet during starvation[24,25], leading to a decrease in circulating/systemic insulin[26]. Using mice fed normally or starved for 10–14 h, we isolated blood, retina and RPE to analyze C-peptide and *Ins2* mRNA (Fig. 2a). Starvation caused C-peptide levels to drop in the blood, yet C-peptide in the retina remained stable (Fig. 2b). Further, *Ins2* mRNA increased 4-6-fold in the RPE under nutrient-poor conditions (Fig. 2b) contrasting with pancreatic *Ins1* and *Ins2* (refs. [25,27]).

To confirm these observations genetically, we used global *Ins2* knockout mice (which avoids partial deletion in the Best1-Cre-$Ins^{2f/f}$ mice). Previous studies have shown that global *Ins2 KO* mice have no defects in systemic blood insulin due to continued expression of *Ins1* in the pancreas[28,29]. RPE from *Ins2* KO mice lacked *Ins2* mRNA (Fig. 2c), without a compensatory increase in *Ins1* (Extended Data Fig. 3a). Consistent with previous reports[28,29], *Ins2* KO mice showed no defects in glucose tolerance test (readout of insulin function) or circulating C-peptide levels (Fig. 2d). When we analyzed the interphotoreceptor matrix (IPM), the extracellular space between the RPE and the retina[30], C-peptide was detectable in control mice during starvation and this was lost in the *Ins2* KO (Fig. 2e). Further, in protein lysates from purified RPE, C-peptide was detected by ELISA in control mice but not *Ins2* KO mice (Fig. 2e). These data demonstrate that RPE-dependent local insulin generation in the eye is due to *Ins2* and is regulated independently of systemic (pancreatic) insulin.

Insulin binds to the insulin receptor (InsR), triggering InsR phosphorylation and upregulation of the glucose transporter type 4 (GLUT4). To probe whether RPE-derived insulin could signal to the retina, we measured InsR phosphorylation and GLUT4 upregulation in the retina of control and *Ins2* KO mice under fed or conditions when systemic insulin is low (starved). InsR phosphorylation was comparable between control and *Ins2* KO mice under fed conditions; however, under starved conditions, InsR phosphorylation as well as GLUT4 were still detectable in the control retina; importantly, this signal was lost in *Ins2* KO mice (Fig. 2f). Thus, RPE-derived insulin promotes insulin signaling in the retina when circulating insulin is low. We observed no difference between control and *Ins2* KO mice in InsR phosphorylation in muscle and adipose tissues (Extended Data Fig. 3b).

As another approach, we treated mice with streptozotocin (STZ), which causes loss of pancreatic β-cells (thereby inducing diabetes) and examined their retinas (Extended Data Fig. 4a). Despite hyperglycemia at 4 weeks after STZ treatment (blood glucose levels of >600 mg dl^{-1} and minimal circulating C-peptide levels, Extended Data Fig. 4b), there was comparable InsR phosphorylation in the retina of untreated and STZ-treated WT mice, in fed or starved states. Further, STZ-treated *Ins2* KO mice had lower InsR phosphorylation (Extended Data Fig. 4c) (the residual InsR phosphorylation may arise from light-induced InsR auto-phosphorylation that is insulin-independent[31]). While the STZ data are consistent with the observations above, we interpret this cautiously, as reports suggests that STZ-induced hyperglycemia can impact retinal homeostasis[10,32].

Phagocytosis upregulates insulin expression by the RPE

RPE-mediated phagocytosis of the POS (around light onset) is necessary for photoreceptor homeostasis[33], as it removes damaged photoreceptors from the previous day[8,9]. To test whether *Ins2* expression in the RPE might be linked to phagocytosis, we first asked whether starvation impacts RPE phagocytosis. Notably, photoreceptor outer segment internalization by the RPE (measured by immunofluorescence on retinal slices) was increased under starvation conditions at ~2 h after light onset, correlating with the reported peak of diurnal phagocytosis[34] (Fig. 3a and Extended Data Fig. 5a). To address this further, we designed and optimized a new flow cytometry-based assay to measure in vivo POS phagocytosis by the RPE (Fig. 3b) that enables scoring thousands of RPE cells for phagocytosed photoreceptor-derived rhodopsin. Starvation/was not due to impaired rhodopsin degradation, as rhodopsin degradation by RPE occurred normally at different time points after light onset (Extended Data Fig. 5b).

Phagocytosis of POS by the RPE starts around light onset, peaks 2 h later and declines throughout the day[34,35]. We isolated eyes from mice at different times and quantified *Ins2* mRNA in the RPE (Fig. 3c). *Ins2* mRNA closely mirrored phagocytosis kinetics, with insulin increasing around light onset (6:00 in our vivarium), peaking 2 h after (8:00) and declining throughout the day (Fig. 3c). InsR phosphorylation and GLUT4 upregulation also changed with time of day, peaking 1 h after light onset (7:00) and declining throughout the day (Fig. 3d); however, in *Ins2* KO mice, the time of day did not affect InsR phosphorylation

or GLUT4 levels in the retina, linking diurnal changes in signaling with local insulin secretion by the RPE.

If RPE phagocytosis were linked to *Ins2* induction, we asked whether this would be affected by loss of specific phagocytic receptors (Fig. 3e). To test this, we first used mice carrying a global deletion of MerTK[17,36], a key phagocytic receptor for RPE phagocytosis[37] (KO strain originally generated by the Lemke group). RPE from the *MerTK* KO mice had near complete ablation of *Ins2* expression (Fig. 3e). Retinas from *MerTK* KO mice also trended toward lower InsR phosphorylation and significantly decreased GLUT4 and C-peptide levels compared to control mice (Extended Data Fig. 5c). As multiple receptors can impact RPE phagocytosis, we also tested mice deficient in another phagocytic receptor CD36 (ref. [38]). RPE from *CD36* KO mice also showed decreased *Ins2* expression (Fig. 3e). The mice used in these studies were of an age when their retinas were morphologically intact without retinal damage[17].

To complement the above studies, we also used a ‘gain of function’ approach. Cleavage of the ectodomain of MerTK on the RPE is one mechanism by which POS phagocytosis decreases over time after light onset[30]. We used a knock-in mouse strain where key cleavage residues within MerTK have been modified, rendering it cleavage-resistant (MerTK$^{CR;}$ Extended Data Fig. 5d)[39]. Notably, RPE from MerTK^{CR} mice displayed an increase in phagocytosis of POS compared to controls (Fig. 3f) and this correlated with greater *Ins2* expression (Fig. 3f). Testing whether insulin itself might promote RPE phagocytosis, we did not detect a difference in RPE phagocytosis between control and *Ins2* KO mice (Extended Data Fig. 5e), suggesting that insulin production was downstream of POS uptake. Collectively, these data demonstrate that phagocytic receptors and diurnally regulated RPE phagocytosis promote *Ins2* gene expression by the RPE.

Linkage of RPE-derived *Ins2* to physiology and disease

The best known physiological effect of insulin on tissues is the stimulation of glucose uptake through GLUT4 upregulation[9]. Induction of local insulin signaling in the retina is most pronounced under starved/low systemic insulin conditions; therefore, we measured glucose uptake in the eye via positron emission tomography (PET). Specifically, starved WT or *Ins2* KO mice were intravenously given radiolabeled [^{18}F]fluorodeoxyglucose (FDG; a non-hydrolysable form of glucose that does not stimulate systemic insulin) and the uptake of [^{18}F]FDG was measured in the eye (Fig. 4a). FDG uptake was decreased in the *Ins2* KO mice compared to control mice (Fig. 4a). To further confirm that this reduction in glucose uptake was attributable to insulin from the RPE, we imaged *Best1*-Cre Ins$^{2f/f}$ mice. Again, FDG uptake was decreased in the eyes of *Best1*-Cre Ins$^{2f/f}$ mice (Fig. 4a). We also performed dynamic PET imaging, which is a qualitative assay performed over time. Using this approach, we again saw a decrease in total signal for FDG and glucose uptake was also slower when measured over time (Fig. 4b, Supplementary Video 1 and Extended Data Fig. 6). To complement PET imaging, we also measured total glucose in the retina of fed and starved mice; again, the global *Ins2* KO mice and *Best1*-Cre Ins$^{2f/f}$ mice exhibited decreased total glucose in the retina under starved conditions (Fig. 4c). Notably, when mice had been fed ad libitum, glucose levels in the retina did not change compared to control

(Fig. 4c). Thus, RPE-derived insulin influences retinal glucose uptake, a key aspect of retinal physiology.

Most of the glucose consumed by photoreceptors is converted to lactate through aerobic glycolysis rather than undergoing oxidative phosphorylation[3]. When we measured lactate under starved conditions, total lactate levels in the retina of *Ins2* KO mice were significantly decreased in both global *Ins2* KO and *Best1*-Cre $Ins^{2f/f}$ mice compared to controls (Fig. 4d). As expected, we did not see a decrease in lactate levels in the retina of mice fed ad libitum (Fig. 4d).

To better understand the impact of RPE-derived insulin on metabolic homeostasis of the retina, we performed untargeted metabolomics on retinas, as well as on purified RPE from control and *Ins2* KO mice under starved/low systemic insulin conditions. Retinas of *Ins2* KO mice showed alterations in >40 metabolites compared to control mice (Fig. 5a). Notably, many of the metabolites decreased in *Ins2* KO retinas are known to be regulated by insulin in other insulin-responsive tissues[40]. Again, lactate came up as a metabolite decreased in the retinas of *Ins2* KO mice (Fig. 5a,b). Another modified pathway in *Ins2* KO mice was amino acid metabolism (Extended Data Fig. 7a,b), with the amino acid serine being one of the metabolites decreased in *Ins2* KO retinas (Fig. 5a,b). Due to high demand for serine in neural tissues, glycolysis-derived serine provides the largest contribution to intracellular serine stores in the retina[41]. Strikingly, retinas of starved *Ins2* KO mice showed both a decrease in serine as well as metabolites that depend on serine for their synthesis, such as glycine and folate cycle-derived methionine[42] (Fig. 5a,b). Thus, loss of local RPE-derived insulin can have a broad impact on retinal metabolism, particularly on metabolites linked to retinal homeostasis. Metabolomics of purified RPE from starved WT and *Ins2* KO mice did not show significant changes in metabolites, suggesting that the RPE-derived insulin may act in a paracrine rather than autocrine fashion (Extended Data Fig. 8a–c).

As another test of retinal physiology, we performed electroretinography (ERG) to measure electrical changes in the retina in response to light, under fed and starved conditions in control and *Ins2* KO mice. In the retina, photoreceptor cells synapse onto bipolar cells and inhibit their electrical activity under dark conditions; in response to light, photoreceptor cells become silenced allowing bipolar cells to become active. This can be observed as the a-wave and b-wave, whose amplitude in the electroretinogram is a measure of photoreceptor and bipolar cell activity, respectively (Fig. 5c). While the b-wave amplitude in control mice remained unchanged in fed versus starved conditions (Fig. 5c), the b-wave amplitude in *Ins2* KO mouse retina significantly increased in starved compared to fed conditions (Fig. 5c). We observed no obvious change in a-wave amplitude in control versus *Ins2* KO mice (Extended Data Fig. 9), likely due to compensatory reasons. These data suggest that *Ins2* KO retinas have a defect in visual processing/response to light under starved conditions.

Retinitis pigmentosa is a human retinal disease characterized by initial degeneration of rod cells, the photoreceptors responsible for overall light sensing, causing night blindness. This is followed by progressive loss of cone cells, which mediate color vision. The combined loss of rods and cones leads to progressive blindness. Death of cone cells has been attributed to defects in glucose homeostasis[4–6]. Independently, defects in light-induced

InsR activation[31,43], as well as downstream signaling pathways[44], have been implicated in cone degeneration. As loss of RPE-derived insulin affects glucose homeostasis and insulin signaling in the eye, we asked whether loss of *Ins2* affects cone viability in the rd1 mouse model of retinitis pigmentosa[4]. For this, we crossed the *Ins2* KO mice to rd1 mutant mice and asked whether cone loss might be increased in the rd1/*Ins2* KO mice. Compared to rd1 mice, cone cell numbers in rd1 *Ins2* KO mice were substantially reduced by 8 weeks (Fig. 5d). These data suggest that RPE-derived insulin is important for maintaining cone viability in a model of retinal disease.

Discussion

The data presented in this work provide several insights. First, multiple orthogonal pieces of evidence reveal RPE cells as a source of local *Ins2* in the retina. Second, insulin produced in the RPE is modulated by phagocytosis (a key function of the RPE), with specific phagocytic receptors linked to RPE phagocytosis influencing *Ins2* induction; this also suggests that failures in RPE-mediated phagocytosis, besides the defective removal of damaged POS, may have broader consequences to metabolic homeostasis of the retina, including serine metabolism. As we were revising this work, a new study[45] reported that the MerTK KO strain used here[17,36] (and also used by numerous investigators over many years) has reduced expression of another TAM receptor, Tyro3. In this study[45], the authors further showed that generically ablating Tyro3 together with conditional deletion of MerTK can phenocopy the retinal deficits characteristic of the original MerTK KO line. Relevant to our current work, although the reduced Tyro3 expression may have contributed to the decreased *Ins2* expression we see in the MerTK KO mice, it is notable that Tyro3 is also a phagocytic receptor. Further, we took two additional orthogonal approaches in our work that further support the notion that phagocytosis is linked to insulin production: the CD36 null mice, which show a decrease in *Ins2* expression and the ‘gain of function’ with the MerTK cleavage-resistant mice that shows an increase in insulin production. Third, while RPE-derived insulin (similar to pancreatic insulin) is important for promoting glucose uptake in the retina, RPE-derived insulin is regulated differently from systemic insulin during starvation and starvation also promotes phagocytosis by the RPE. Of note, multiple previous studies have noted the retina as insensitive to systemic insulin[11,12]. Our data suggest that insensitivity of the retina to systemic insulin may in part arise from local insulin produced by the RPE. Fourth, in mice lacking *Ins2* (with normal circulating glucose levels via continued expression of *Ins1*), there is exacerbated cone death in a mouse model of retinitis pigmentosa, highlighting the importance of RPE-derived insulin in mitigating retinal degeneration. In our studies we found that the human retina also produces insulin; however, there are no reports of the RPE being a target of autoimmune destruction in type 1 diabetes. As the retina is considered to be immune privileged, one aspect of future research will be to address how the local insulin production in the eye may impact autoimmune outcomes in type 1 diabetes. Collectively, the data presented in this work advance the concept that the RPE provide a local source of insulin in the eye and this has functional relevance to retinal physiology, retinal metabolic homeostasis and in limiting retinal disease.

Methods

Reagents

The reagents used for different parts of this work were obtained from the indicated suppliers as follows: RNAProtect cell reagent (QIAGEN, 76526), NucleoSpin RNA isolation kit (Macherey Nagel, 740955), Quanti-Tect reverse transcription kit (QIAGEN, 205313) and Taqman probes (Thermo Fisher): *Ins2* (Mm00731595_gH), *Mer* (Mm00434920_m1), *rhodopsin* (Mm01184405_m1) and *Ins1* (Mm01950294_s1). Antibodies used were anti-insulin (Agilent, IR002), anti-insulin (Cell Signaling, 3014), anti-C-peptide (Phoenix Pharmaceuticals, H-035-03), anti-Cre recombinase (Millipore, MAB3120), anti-rhodopsin (Abcam, ab98887), anti-cone arrestin (Millipore, AB15282), anti-phospho insulin receptor-β (Tyr1150/1151) (19H7) (Cell Signaling, 3024), anti-insulin receptor-β (Novus Biologicals, NBP2 12793), anti-Glut4 (Alomone Labs, AGT 024), anti-β actin HRP (Sigma, A3854) and anti-rabbit IgG HRP (GE Healthcare, NA934V). We also used Halt Phosphatase inhibitor (Thermo Fisher, 1862495), Halt Protease inhibitor (Thermo Fisher, 1862209), ultrasensitive mouse insulin ELISA (Mercodia, 10-1249-01), mouse C-peptide ELISA (CrystalChem, 90050), rat/mouse C-peptide 2 ELISA (Millipore, EZRMCP2), glucose Glo Assay (Promega, J602), lactate Glo Assay (Promega, J5021) and eBioscience Foxp3 Transcription Factor Staining Buffer Set (Thermo Fisher, 00-5523-00).

Mice

Mice were housed in a vivarium with a 14-10-h light–dark cycle, with lights on at 6:00 and turning off at 20:00. They receive an ad libitum diet (unless otherwise noted for individual experiments) of regular chow and are kept at 72 °F and 40% humidity. C57BL/6J, *Best1*-Cre (strain 017557), $^{YFPflox\text{-}stop\text{-}flox}$ (strain 006148), *rhodopsin*-Cre (015850), *CD36* KO (strain 019006) and Rd1 (strain 000656) mice were acquired from Jackson Laboratories and bred in our facilities. MerTK KO mouse strain[36] was acquired from Jackson Laboratories (strain 011122) and backcrossed to C57BL/6J for six generations. Controls for MerTK KO and *CD36* were WT littermates. $Ins^{2f/f}$ mice[46] were generated as previously described and were crossed to *Best1*-Cre or *rhodopsin*-Cre[47] strains. Controls for these mice were *Best1*-Cre, *rhodopsin*-Cre and/or $Ins^{2f/f}$. *Ins2* KO mice used in these experiments came from a mix of $Ins^{2f/f}$ crossed to E2A-Cre (from Jackson Laboratories) in which progeny were selected for global loss of $Ins^{2f/f}$ and were then backcrossed to C57BL/6J to remove E2A-Cre or from *Nod*.I*ns2*^{null} (Jackson laboratories) backcrossed to C57BL/6J for four generations (diabetes in NOD mice predominantly affects females and autoimmunity is lost with just one backcross). Control for these mice were C57BL/6J for $Ins^{2f/f}$ and WT littermate control for Ins^{2null}. Mer cleavage-resistant mice have been described previously[39]. Controls for these mice were WT littermates. Rd1 mice were crossed to Ins^{2null} mice and Rd1 littermates were used as controls. Rd1 and Rd1 Ins^{2null} were then dissected at 8 weeks of age. Only male mice were used in these experiments. All animals were killed between 9–12 weeks; two exceptions were MerTK KO mice (and respective controls), which were killed at 4 weeks of age before onset of any retinal complications, and *Ins2* KO (and control) used for metabolomics, which were killed at 10–18 weeks. All animal procedures were approved by and performed according to guidelines of the Institutional Animal Care and Use Committee at the University of Virginia.

Gene expression analysis

RNA isolation for RPE.—Isolation of RPE for gene expression analysis was conducted as previously described with a few modifications[48]. Mice were killed with CO_2 and eyes were enucleated. Eyes were then further dissected in ice-cold PBS to carefully remove lens, cornea, iris and retina. The eye cup (containing RPE/sclera/choroid) was then moved toa microcentrifuge tube containing 100 μl of ice-cold RNAProtect cell reagent and left on ice for 20 min. During this time, a tube containing the eye cup was gently tapped at intervals of 5 min. After, the eye cup was removed and cells were spun at 4 °C for 5 min at 700*g* leaving an RPE pellet behind. RNAProtect cell reagent was removed and subsequent RNA isolation was performed using the NucleoSpin RNA isolation kit (Macherey Nagel).

Nuclear isolation from RPE and RNA extraction.—RPE cells were isolated as previously described[49]. YFP^+ RPE cells were sorted with a FACS Aria Fusion cell sorter. Cells were then spun down at 1,000*g* for 5 min at 4 °C and hydrated in 1 ml cells lysis buffer with protease inhibitors (1% Tween40, 2 mM $MgCl_2$, 10 mM β-glycerophosphate, pH 7 and 5% glycerol) and incubated for 5 min on ice. Thereafter 1 ml water was added and cells were again incubated for 5 min on ice. Cells were then broken up with a glass Dounce homogenizer using a tight inserting pestle until nuclei were liberated. Lysates were layered on top of a two-step sucrose cushion containing 20 ml lower cushion (500 mM sucrose, 2 mM $MgCl_2$, 25 mM KCl, 65 mM β-glycerophosphate, pH 7 and 5% glycerol) and 10 ml upper cushion (340 mM sucrose, 2 mM $MgCl_2$, 25 mM KCl, 65 mM β-glycerophosphate, pH 7 and 5% glycerol), spun down at 1,000*g* for 10 min at 4 °C and supernatant was discarded. Crude nuclei were resuspended in a desired amount of upper cushion solution. Subsequent downstream RNA isolation was performed using the NucleoSpin RNA isolation kit (Macherey Nagel).

RNA Isolation for other tissue.—All other tissue except retina were dissected and homogenized using a PRO200 homogenizer (Proscientific). Retinas were homogenized by pipetting up and down with a p200 pipetman. After homogenization, subsequent downstream RNA isolation was performed using the NucleoSpin RNA isolation kit (Macherey Nagel).

Primary RPE cell culture RNA isolation.—Primary RPE cell culture was performed as previously described[49]. RPE and immortalized mouse embryonic fibroblasts were then grown for 2–4 weeks, after which homogenization and RNA isolation was performed using the NucleoSpin RNA isolation kit (Macherey Nagel).

RT–PCR.—Complementary DNA synthesis was performed using Quanti-Tect reverse transcription kit (QIAGEN). FC and expression-level gene analysis for target and housekeeping genes was performed using Taqman probes (Applied Biosystems) run on a StepOnePlus Real Time PCR System (Applied Biosystems).

Retinal cryotissue sections for RNAScope and IHC

Mice were killed with CO_2 and eyes were enucleated. Retinal tissue cryosections were prepared from enucleated eyes as previously described[50]. RNAScope was performed

using the V2 Multiplex-Fluorescent assay (ACDbio) per manufacturer's instructions. Immunohistochemistry (IHC) was performed as previously described[50]. Representative images were taken using a Zeiss LSM 880 confocal microscope.

RPE protein isolation and analysis

Protein isolates from RPE were obtained as previously described[51]. Insulin ELISA was performed per manufacturer's instructions using Ultrasensitive Mouse Insulin ELISA (Mercodia). C-peptide ELISA was performed as per manufacturer's instructions using the Mouse C-peptide (CrytalChem) and Rat/Mouse C-peptide 2 (Millipore) ELISA kits.

KCl induced release of insulin in the eye cup

Eyes were enucleated and retinas were removed from the eye cups in Krebs–Ringer–bicarbonate–HEPES buffer (KRB). Eye cups were then incubated in fresh KRB at 37 °C for 5 min, KRB was removed and replaced with fresh KRB at 5 mM or 50 mM KCl concentration for 10 min at 37 °C. Supernatant was collected and then probed for C-peptide-2 through ELISA.

Human tissue samples

De-identified human surgical enucleation specimens were obtained from the University of Virginia Department of Pathology archives via the auspices of the University of Virginia Biorepository and Tissue Research Facility. A protocol for utilization of de-identified archival paraffin-embedded specimens was approved by the University of Virginia Institutional Review Board. Informed consent from donors was waived. All staining on human tissue samples used formalin-fixed, paraffin-embedded tissue sections.

Inter photoreceptor matrix protein isolation

Mice were killed with CO_2 and eyes were enucleated on a dry dish. Lens and vitreous humor were then dissected out and then the retina was delicately separated from the rest of the eye cup. Soluble proteins from the retina interphotoreceptor matrix of each retina were washed out in 80 µl of HBSS without $Ca2^+/Mg2^+$ with protease and phosphatase inhibitors for 20 min on a shaker (500 r.p.m.) at 4 °C. Isolate was then centrifuge at 14,000*g* for 5 min at 4 °C. Supernatant was then collected and subsequent C-peptide ELISA (CrystalChem) was performed as per manufacturer's instructions. Results were normalized to the protein concentration from each supernatant.

Glucose tolerance test

Dextrose (1.5 g kg^{-1}) was prepared, sterile filtered and injected intraperitoneally. The glucose excursion was monitored over a 2-h time course and compared between genotypes. Tail vein blood samples were analyzed by glucometer (OneTouch Verio Flex) at 0, 15, 45, 60 and 120 min following dextrose injection. The cumulative glycemic excursion was evaluated as the area under the curve.

Immunoprecipitation

Equal amounts of protein lysate were incubated overnight at 4 °C with anti-insulin receptor-β antibody (10 g mg^{-1} lysate, Novus Biologicals, NBP2 12793) and pre-washed SureBeads Protein G Magnetic Beads (Bio-Rad). Unbound protein and antibody were removed, and protein bead complexes were washed per manufacturer instructions. Bound protein was eluted in Laemmli sample buffer containing β-mercaptoethanol and incubated at 70 °C for 10 min.

Immunoblotting of retina, muscle and fat

Protein lysates were prepared from isolated tissue using RIPA lysis buffer with added Halt Protease and Phosphatase Inhibitor Cocktail (Thermo Scientific). Equal amounts of protein lysate were loaded in TGX Precast gels (Bio-Rad) or in-house-made 7% polyacrylamide gels, then subjected to SDS–PAGE. Protein was transferred onto PVDF membranes using the Trans Blot Turbo transfer system (Bio-Rad). After transfer, blots were blocked for 1–3 h in 5% dry milk in TBST at room temperature, then probed using anti-phospho insulin receptor β (Tyr1150/1151) (19H7) (1:1,000 dilution, Cell Signaling, 3024), anti-insulin receptor β (1:5,000 dilution, Novus Biologicals, NBP2 12793), anti-Glut4 (1:1,000 dilution, Alomone Labs AGT, 024), anti-β actin HRP (1:15,000 dilution, Sigma, A3854) and Amersham ECL anti-rabbit IgG HRP (1:5,000 dilution, GE Healthcare, NA934V). In some experiments, primary and secondary antibodies were diluted in SignalBoost Immunoreaction Enhancer kit solutions (Millipore Sigma). Blots were exposed using Western Lightning Plus ECL kit (PerkinElmer) or SuperSignal West Femto ECL kit (Thermo Scientific). Images were collected on the ChemiDoc Touch imagining system and analyzed using ImageLab software (Bio-Rad).

Streptozotocin treatment

Diabetes was induced by intraperitoneal injections of a freshly prepared solution of STZ in 0.1 M citrate buffer (pH 4.4) at 60 mg kg^{-1} body weight once a day for 5 d in male mice at 4–6 weeks of age. Control mice were injected with only citrate buffer. Diabetic mice were then maintained for 4 weeks after the last injection of STZ before retinas were dissected and processed for immunoprecipitation. All diabetic mice processed for this experiment had non-fasting glucose levels >600 mg dl^{-1}.

RPE dissociation and phagocytosis assay with flow cytometry

Mice were killed with CO_2 and eyes were enucleated. Eyes were then further dissected in ice-cold PBS to carefully remove lens, cornea, iris and retina. The eye cup (containing RPE/sclera/choroid) was then moved to a microcentrifuge tube containing 100 µl of 200 U ml^{-1} of pre warmed Collagenase IV. The microcentrifuge containing the eye cup was then submerged in 37 °C water bath for 12 min and the tube was gently tapped every 2 min. After, the reaction was quenched in flow cytometry sample buffer and the eye cup was removed. Microcentrifuge tube containing dissociated RPEs was then spun at 400*g* at 4 °C for 5 min. Supernatant was removed and cells were treated with fixation solution (100 µl) from Foxp3 eBio kit (1:4 fixative:diluent) for 30 min room temperature. Cells were subsequently washed with permeabilization buffer (Foxp3 eBio kit) 1:10 in

dH_20, resuspended in permeabilization buffer for 15 min and then incubated with anti-rhodopsin antibody at 4 °C for 1 h. Cells were then spun at 400*g* for 5 min, washed 1× in permeabilization buffer and then incubated with secondary antibody for 30 min. Cells were then washed 1× with permeabilization buffer, 1× with flow cytometry sample buffer and finally resuspended in flow cytometry sample buffer. Cells were then run on a AttuneNxT Flow Cytometer. The gating strategy used is shown in Supplementary Fig. 1.

RPE phagocytosis analysis using IHC

Retinas from starved and fed mice dissected 2 h after light onset were stained with anti-rhodopsin (Abcam). Imaging was conducted with a Zeiss Axio Observer and quantification was performed using ImageJ. Quantification of phagocytosis was measured by the amount of rhodopsin immunoreactivity in the RPE divided by pixels (middle panel) and presented as phagosomes per area on the y axis. Quantification of the number of phagosomes in RPE was done by counting rhodopsin puncta in the RPE (right). A representative image was taken using a Zeiss LSM 880 confocal microscope.

PET imaging

All mice were fasted overnight the day before PET/CT scan. The mice were anesthetized using isoflurane and oxygen mixture (inhalation anesthesia, 5% ratio during induction, later reduced to 2%). The animals were given [^{18}F]FDG (4.0 ± 2.8 MBq) via intraperitoneal injection. After a 45-min injection, static PET/CT imaging was performed for 15–20 min followed by a 10-min CT scan using the Albira Si small animal tri-modal PET/CT/SPECT scanner (Bruker). PET images were reconstructed as previously described[52]. Image co-registration and analysis was performed using PMOD 4.1 (PMOD Technologies). Averaged standard uptake values (SUVs) were derived for each volume of interest (VOI) and data are reported as percent injected dose per ml (%ID ml^{-1}). Datasets were fully corrected for random coincidences, scatter and attenuation. Images were smoothed with a Gaussian filter (1.35 mm in both directions).

PET image data analysis

The images were normalized as SUVs using the formula SUV = decay of the corrected mean tissue activity concentration (Bq ml^{-1}) / (injected dose (Bq) × body weight (g)). A VOI was manually drawn around left and right retina using PMOD 4.1, Pview. The maximal SUV was calculated for the corresponding VOIs. To control for potential effects of insulin ablation on total glucose levels, values were similarly obtained for the liver and retina and the values were then normalized to those of the liver. The normalized values are those presented in Fig. 4 as a percent uptake relative to WT.

Dynamic PET imaging

Mice were imaged using Albira Si Tri-modal PET/SPECT/CT scanner. The Albira PET imager is a three-ring scanner with an axial field of view (FOV) of 150 mm and transaxial FOV of 80 mm. The volumetric spatial resolution of the PET system ranges from 0.41–0.87 mm^3 at the axial center with a sensitivity of 11% at the center of the FOV. The noise equivalent count rate for the mouse phantom was measured to be 486 kcps at 23

MBq. Dynamic FDG PET imaging of the mice were performed using a similar protocol as described earlier[53]. Rate of FDG uptake, Ki (and kinetic rate constants) and total blood volume were computed in MatLab (MathWorks) as described previously[54].

Retina whole glucose and lactate luciferase assay

Mice were killed with CO_2 and eyes were enucleated. Lens and vitreous humor were then dissected out and then the retina was delicately separated from the rest of the eye cup. Retinas were then processed and analyzed with Promega Glucose or Lactate Glo luciferase kit per manufacturer's instructions. A lactate value in the *Best1*-Cre $Ins^{2f/f}$ dataset was thrown out due to extreme variability.

Metabolite extraction

Mice were fasted overnight and killed with avertin after light onset. Five replicates each of both retinal and RPE tissues (from WT and KO mice) were collected and dissected, flash frozen and stored at −80 °C until extraction. Tissues were thawed on ice. Approximately 400 μl of cold methanol was added to along with four steel balls (Fischer Brand; diameter 2.4 mm) and shaken vigorously in Fischer Brand Bead Mill 24 at speed of 5 Hz, three cycles of 20 s each with 10 s rest. Tubes were further vortexed and shaken at 900 r.p.m. for 30 min at 4 °C in temperature controlled thermal shaker. After adding 200 μl of chloroform and 400 μl of water, the top aqueous phase was recovered as metabolite mixture. Metabolite extract was dried overnight in speedVac and reconstituted in 100 μl of 0.1% FA. A total of 10 μl from each tube was removed to create a pooled quality control (QC) sample that was injected at the beginning and end of the mass spectrometry (MS) sequence and additional QC samples were injected after every five sample injections.

Untargeted metabolite analysis

Untargeted metabolite analysis was performed on a Thermo Orbitrap IDX Tribrid MS at Biomolecular Analysis Facility, University of Virginia, School of Medicine. Samples were transported to the MS via a Thermo Vanquish UHPLC and separation of the polar metabolites was achieved using Waters BEH C18 column (Waters Corp; 2.1 × 150 mm; 1.7 μm) maintained at 30 °C. A conventional data-dependent acquisition mode was used for data acquisition and samples were randomized during extraction and analysis on the mass spectrometer. The injection volume was 5 μl. For the 15-min gradient, the standard mobile phase for RPLC was Buffer A = 0.1% formic acid in water and Buffer B = 0.1% formic acid in methanol in electrospray ionization (ESI) positive and negative mode. The linear gradient elution was as follows: 0–8 min 50% B, 8–13 min held at 98% B, and 13.1–15.0 min revert to 0% B to re-equilibrate for the next injection. ESI source conditions were set as follows: ion source type was H-ESI; positive ion voltage was set at 3,500 and negative was set at 2,500. Sheath gas was set at 35 and auxiliary gas was set at 7. Ion transfer tube temperature was set at 275 °C and vaporizer temperature was set at 320 °C.

Data were acquired in full MS mode (1 μscan) at a resolution of 120,000 with a scan range of 67–1,000 m/z at a normalized AGC target of 25% and 50 ms of maximum injection time was allowed. RF lens amplitude was set at 35%. Tandem MS/MS performed by applying quadrupole isolation with an isolation window of 1.6 m/z. Activation type was

set at HCD and masses were fragmented with HCD Assisted Collision Energy (%) of 15,35,50. Fragment masses were detected by Orbitrap at a resolution of 30,000. A total of 20 × 2 sample runs (negative and positive mode), ten QC runs (5 × 2 negative and positive mode) and 4 × 2 blanks (negative and positive) tandem MS/MS runs were acquired. Thermo *.RAW files were converted to an Open Source *.mzML format using msConvert software (http://proteowizard.sourceforge.net/download.html) and brought into MS-DIAL software for analysis (http://prime.psc.riken.jp/compms/msdial/main.html)[55,56].

MS-DIAL analysis parameters were as follows: MS1 tolerance was set at 0.01 Da and Ms2 tolerance at 0.025 Da. Data were collected from 0–15 min at a mass range from 50–1,000 Da. Peak detection was performed with a minimum peak height of 1×10^5 and mass slice width of 0.1 Da. Metabolites were identified by searching the MS2 spectra in the MS-DIAL public database (290,915 records for positive and 36,848 entries for negative mode; v.14) using a mass tolerance of 0.01 Da for MS1 and 0.05 Da for MS/MS with identification score cutoff of 60%. Additionally, peaks were also searched against a library from IROA Technologies (in both positive and negative mode) with a mass tolerance of 0.01, identification cutoff of 90% and RT tolerance of 0.5 min (MS Metabolite Library of Standards; http://iroatech.com/). For peak alignment maximum retention tolerance was set at 0.2 min. Alignment data for all the samples with annotated and unknown identification was exported to MS-CleanR R package (refs. [54,55]). Using MS-CleanR blank injection signal subtraction, background ion drift removal and unusual mass defect filtering, peaks with relative s.d. threshold >30% based on QC were removed. Further data were manually examined and curated to remove duplicates and identification was confirmed based on MS-Finder (using a formula and structure search). Further data processing for statistical analysis, univariate and multivariate analysis was performed in R.

Electroretinography

ERG was performed as previously described[57]. Briefly, scotopic ERG was performed on 13-24-week-old mice. Mice were dark-adapted overnight before the experiments and anesthetized by intraperitoneal injection of 100 mg kg^{-1} ketamine hydrochloride. The pupils were dilated with tropicamide (1%) and phenylephrine (2.5%) eye drops. ERG was recorded using a Ganzfeld ERG (Phoenix laboratories). Scotopic combined responses were obtained using the LabScribe software (Phoenix Laboratories) under dark-adapted conditions (no background illumination, 0 cd m^{-2}) in response to white-flash stimuli ranging from −1.7 to 1.0 log cd s m^{-2} with 20 responses averaged for each stimulus. The amplitude of b-wave was measured as the difference between the a-wave min and the b-wave max.

Retina whole mounts for Rd1 and Rd1 *Ins2* KO mice

Mice were killed with CO_2 and eyes were enucleated. Retinal tissue cryosections were prepared from enucleated eyes as previously described[50]. IHC using cone arrestin antibodies was performed as previously described[50]. Imaging was conducted with a Leica DMi 8 Thunder/TIRF microscope and quantification of the number of cones in the center retina was performed using ImageJ. The center retina was defined as a 1-mm diameter circle with the optic nerve in the center.

Statistical analysis

All box and whiskers plots show minimum to maximum with all independent replicates included, the horizontal line within the box depicting the median and the box extending from the 25th to 75th percentiles. Statistical tests were performed using GraphPad Prism v.8 as indicated in figure legends. Outlier data points were identified using the ROUT method with Q = 1%, with the exception of Extended Data Fig. 4b, where Grubbs with an α of 0.2 was used. No statistical tests were used to determine sample size.

Reporting summary

Further information on research design is available in the Nature Portfolio Reporting Summary linked to this article.

Extended Data

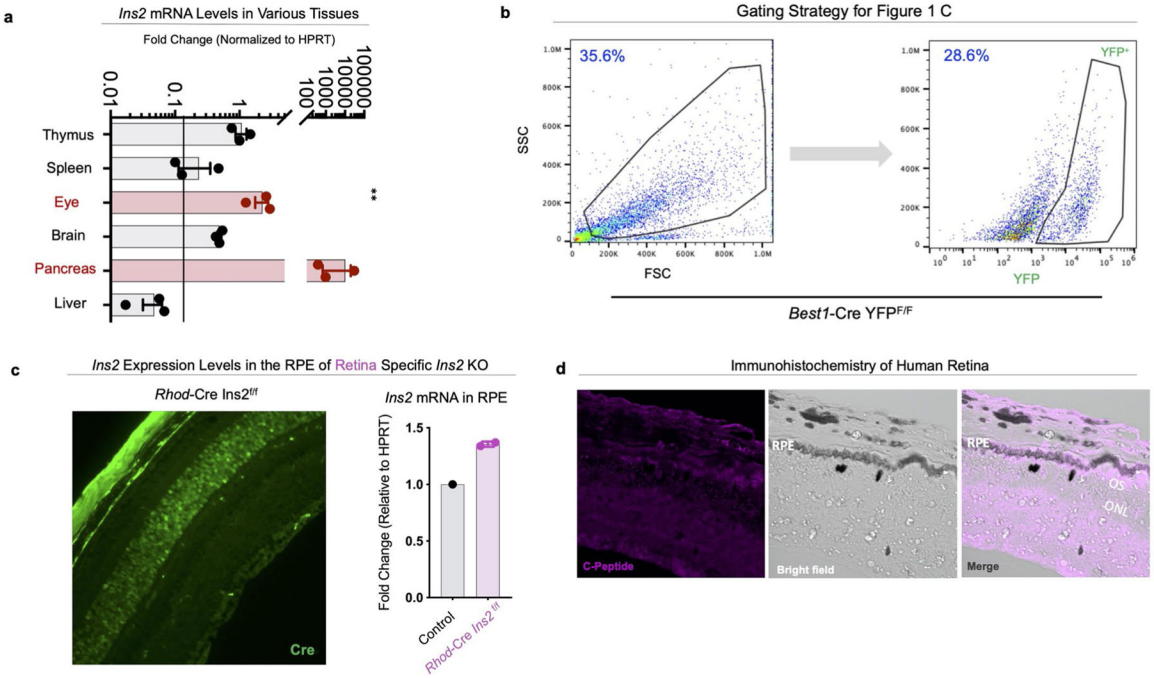

Extended Data Fig. 1 |. Expression of *Ins2* mRNA and Protein Within the RPE Cells of the Eye.
a. RT–PCR of *Ins2* from mRNA isolated from different mouse tissues. n = 3 mice used for each tissue. **p < .01, one-way ANOVA on ranks. b. Flow cytometry panels showing YFP^+ gating strategy for isolated RPE from *Best1*-Cre/$YFP^{flox\text{-}STOP\text{-}flox}$ mice. c. Representative image of two independent experiments showing immunofluorescence analysis at 40x magnification on mouse retina from *Rhodopsin*-Cre $Ins2^{f/f}$ mice using antibodies against Cre (green) (left). RT–PCR of *Ins2* mRNA in RPE of *Rhodopsin*-Cre $Ins2^{f/f}$ shows no change in the expression of the *Ins2* transcript compared to control (right). n = 2 mice used for each genotype. d. Representative image of immunofluorescence analysis at 60x magnification on human retina using antibodies against C-peptide (magenta) with brightfield microscopy. Merge shows that C-peptide, a byproduct of insulin secretion and a metric of insulin release, is present and located in the retina. Plots are presented as in Fig. 1.

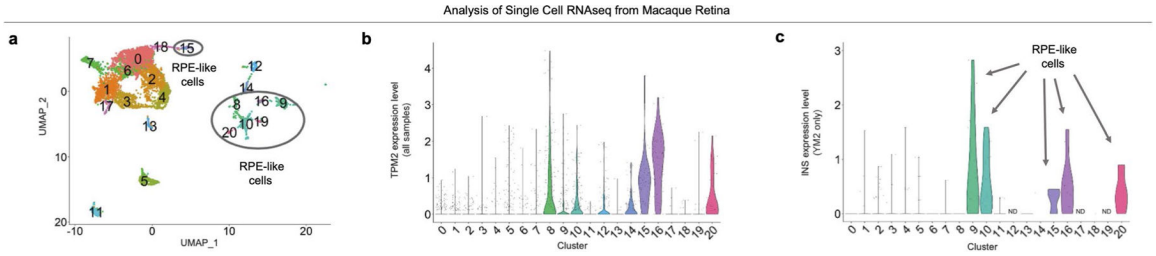

Extended Data Fig. 2 |. Data Mining / Reanalysis of scRNAseq Data from Macaque Retinas Reveals *Ins2* mRNA Expression in RPE and RPE-like Cells.

a. UMAP plot showing different cell types with the RPE-like cell clusters labeled. b. Violin plot showing normalized expression levels of TPM2, a RPE cell gene marker, for all samples. The clusters with the highest TPM2 expression overlay with the clusters we defined as containing RPE-like cells. c. Violin plot showing normalized expression levels of INS in one young male monkey sample (YM2). The detectable expression of INS in YM2 was restricted to RPE-like cells.

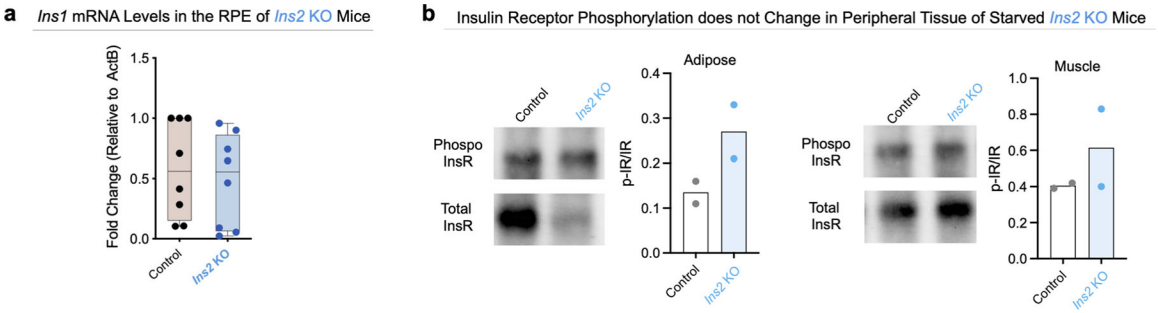

Extended Data Fig. 3 |. *Ins1* mRNA and Insulin Receptor Phosphorylation in *Ins2* KO mice.

a. RT–PCR of *Ins1* fold change in mRNA of isolated RPE from control and *Ins2* KO mice. n = 8 mice used for each genotype. b. Insulin receptor was immunoprecipitated from various tissue lysates of control and *Ins2* KO mice that were starved overnight. Phosphorylation status of the InsR was probed using phospho-specific InsR antibodies via immunoblotting and quantified as the ratio of p-InsR to total InsR. n = 2 mice for control vs *Ins2* KO. Plots are presented as in Fig. 1.

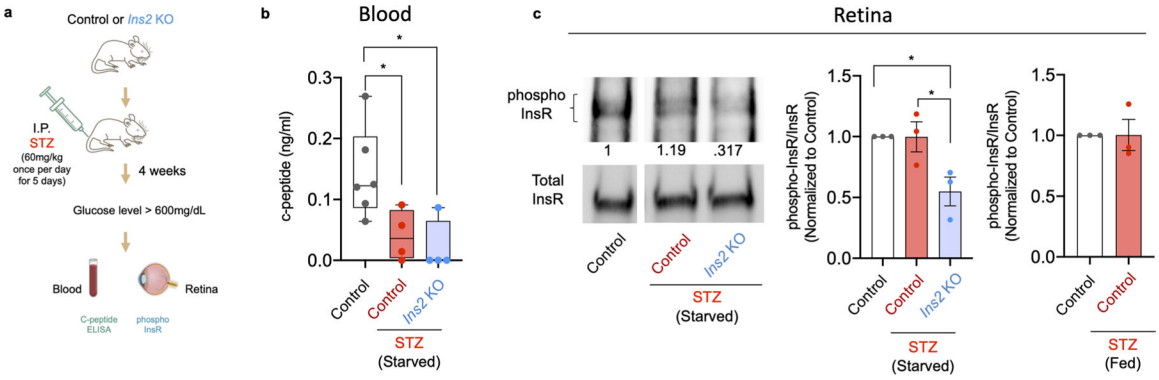

Extended Data Fig. 4 |. InsR Phosphorylation Decreases in the Retina of *Ins2* KO, but not Control, Streptozotocin (STZ) Treated Mice.

a. Schematic of streptozotocin (STZ) treatment. b. ELISA measuring C-peptide levels in blood of control, control STZ-treated, and *Ins2* KO STZ-treated mice starved mice. N = 6 mice for control and N = 4 mice for STZ-treated Control and STZ-treated *Ins2* KO. *p < .05, one-way ANOVA with Dunnet's multiple comparisons test. c. Insulin receptor (InsR) was immunoprecipitated from retina tissue lysates of control, control STZ-treated, and Ins2KO STZ-treated mice, starved overnight (left) or control and control STZ-treated mice fed ad libitum (right). Phosphorylation status of the InsR was probed using phospho-specific antibodies (Tyr1150/1151) via immunoblotting and quantified as the ratio of p-InsR to total InsR, normalized to untreated WT mice. N = 3 mice for all conditions. *p < 05, one-way ANOVA with Tukey's multiple comparison's test. Plots are presented as in Fig. 1.

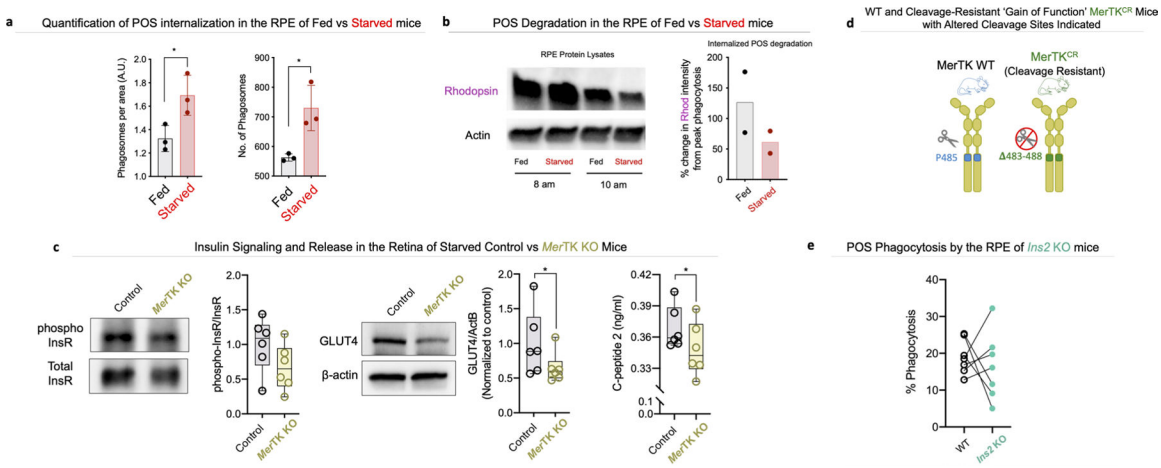

Extended Data Fig. 5 |. RPE Phagocytosis Increases in Starved Mice vs Fed and is not Changed in *Ins2* KO Mice.

a. Quantification of OS phagocytosis by the RPE 2 hours after light onset using immunohistochemistry. Quantification of phagocytosis was measured by the amount of Rhodopsin immunoreactivity in the RPE divided by pixels and presented as phagosomes per area on the y-axis (left). Quantification of the number of phagosomes in RPE was done by counting Rhodopsin puncta in the RPE (right). n = 3 mice used for each condition. *p ≤ .05 paired two-tailed t-test. b. Western blot against Rhodopsin on isolated RPE protein lysates from fed and starved mice at 8 am and 10 am (left). Right panel is quantification of the blot to evaluate POS degradation showing 10 am band intensity as a percent of 8 am (peak phagocytosis) band intensity (right). n = 2 mice used for each time point. c. Insulin receptor was immunoprecipitated from lysates of retina from control and *Mer*TK KO mice that were starved overnight. The lysates were probed for InsR phosphorylation or GLUT4 levels by immunoblotting. C-peptide 2 levels were determined by ELISA. N = 6 mice for each condition. *p < .05 paired two-tailed t-test. d. Schematic of WT and cleavage-resistant 'gain of function' MerTK^{CR} mice with altered cleavage sites indicated (left). e. Phagocytosis quantification of ingested photoreceptor outer segments using flow cytometry on isolated RPE stained with antibody against rhodopsin from Control and *Ins2* KO mice two hours after light onset. n = 7 mice used for each genotype. Plots are presented as in Fig. 1.

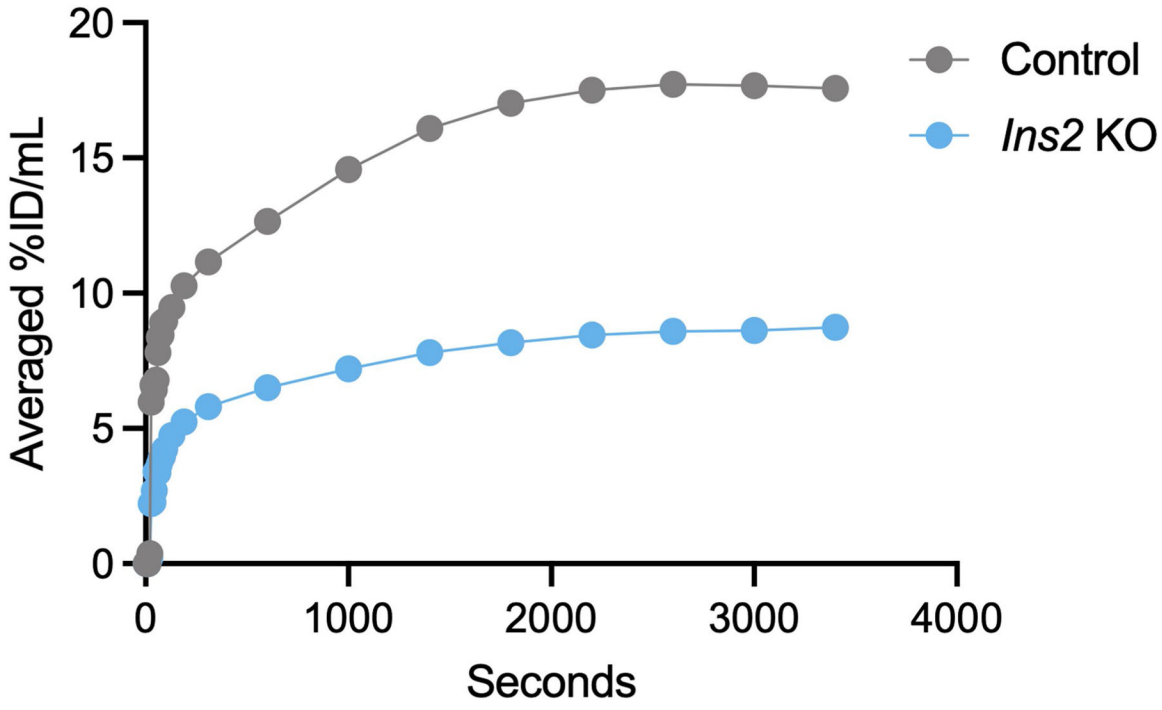

Extended Data Fig. 6 |. Loss of *Ins2* leads to decreased eye glucose uptake as measured by Dynamic *in vivo* PET.

a. Quantification of Dynamic *in vivo* PET imaging for ^{18}[F]FDG glucose uptake in the eyes of control and *Ins2* KO mice after ^{18}[F]FDG injection.

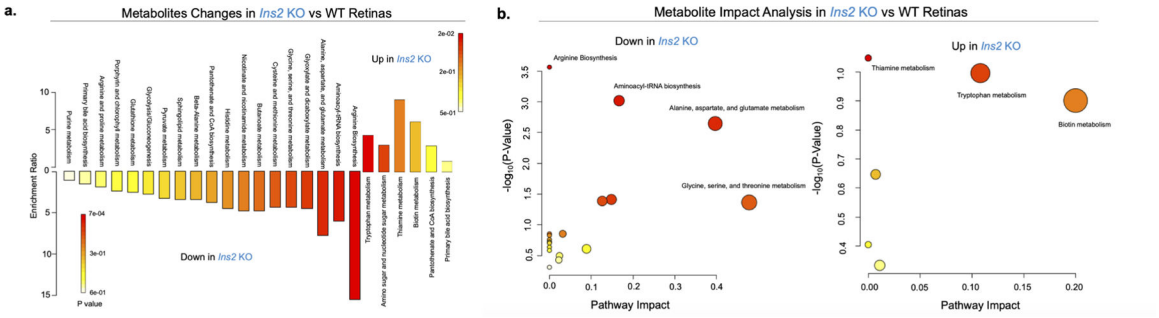

Extended Data Fig. 7 |. Untargeted Metabolomics Reveals Changes in Global Metabolism of Retinas from WT vs *Ins2* Knockout Mice.

a. Enrichment analysis of metabolites from untargeted metabolomics for control over *Ins2* KO retinas (using KEGG database). Data are representative of four biological replicates.

b. Impact analysis of specific metabolic pathways down (left) and up (right) in control vs *Ins2* KO retinas using KEGG database. Pathway significance was determined using Fisher's Exact Tests.

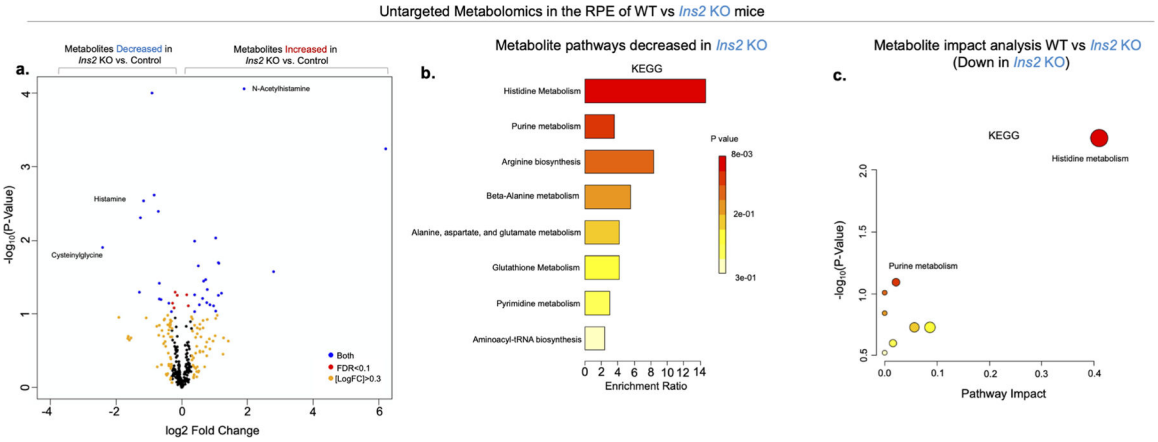

Extended Data Fig. 8 |. Untargeted Metabolomics of RPE from WT and *Ins2* Knockout Mice reveals Minimal Changes in Global metabolism.

a. Volcano plot from untargeted metabolomics of RPE representing statistically enriched or reduced metabolites in the RPE of control mice relative to those of *Ins2* KO using Fisher's exact test. False Discovery rate (FDR, $p < 0.1$) is shown in red, absolute value of the Log_2 fold change of 0.3 (1.2 fold change) in orange, and those in blue meet both criteria. Data are representative of 4 biological replicates. b. Enrichment analysis of metabolites using KEGG database from untargeted metabolomics for control over *Ins2* knockout RPE cells. c. Impact analysis of specific metabolic pathways in control vs *Ins2* KO RPE using KEGG database. Pathway significance was determined using Fisher's Exact Tests.

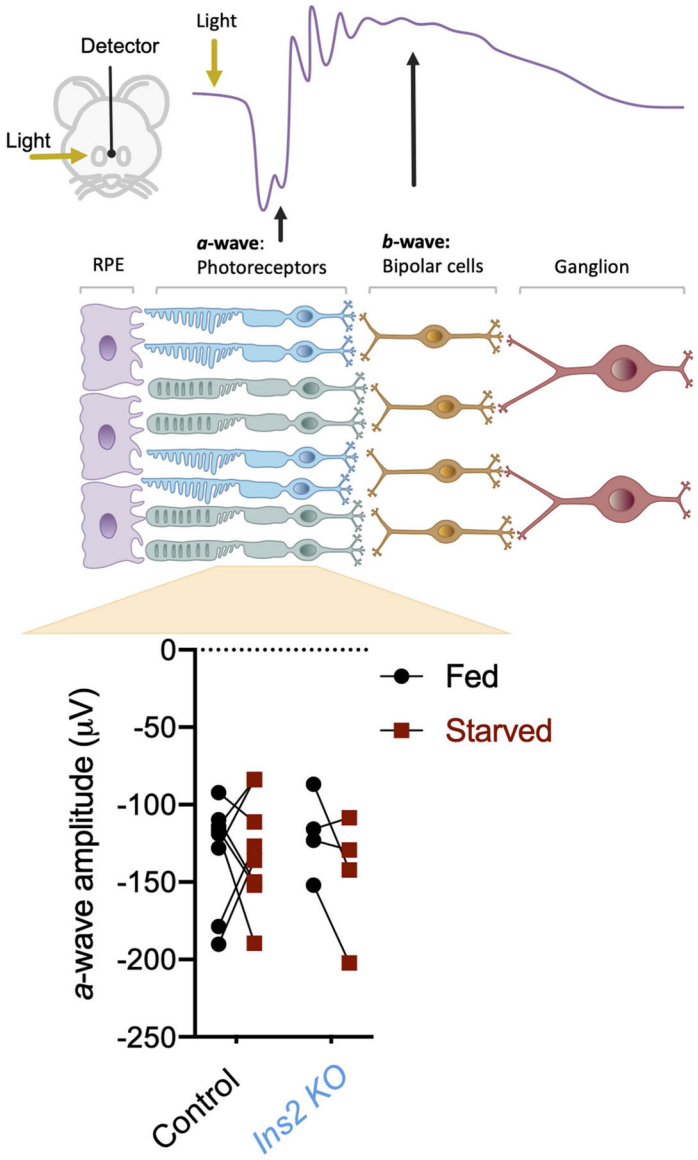

Extended Data Fig. 9 |. *a*-wave Amplitude in the Retina of Fed. or Starved Control and *Ins2* KO Mice.

a. Schematic of scotopic electroretinogram (ERG) on mouse retina to detect visual processing in response to light (top). Quantification of a-wave amplitude in ERG of WT and *Ins2* KO mice under fed and starved condition (bottom). n = 8 mice for WT, n = 4 mice for *Ins2* KO mice.

Supplementary Material

Refer to Web version on PubMed Central for supplementary material.

Acknowledgements

We thank members of the Ravichandran laboratory as well as B. Gelfand and R. Lindsay for input and critical reading of the manuscript. We thank E. Thorpe and I. Tabas for the MerTK^{CR} mice, J. Mandell for human

retinal samples and E. Nandrot and R. Rajala for advice on specific protocols. Figure schematics were created using BioRender images as templates. This work was supported by grants to K.S.R. from the National Institute of General Medical Sciences (R35GM122542), National Institute of Allergy and Infectious Diseases (R01AI159551), the National Heart, Lung and Blood Institute (P01HL120840), the Center for Cell Clearance/University of Virginia and Bone and Joint Canada Investigator funds from the Washington University School of Medicine to J.I.E. via NEI F32 (EY031211) and T32AI7496-23. J.A. is a cofounder of DiceRx, iVeena Holdings, iVeena Delivery Systems, and Inflammasome Therapeutics; has been a consultant for Abbvie, Boehringer-Ingelheim, Olix Pharmaceuticals, Retinal Solutions, and Saksin LifeSciences; and is named as an inventors on patent applications filed by his university, all unrelated to this work. J.A. has received support from the UVA Strategic Investment Fund, National Institutes of Health (NIH) grants (R01EY028027, R01EY029799, R01EY031039, R01AG082108), DuPont Guerry, III, Professorship, and a gift from Mr. and Mrs. Eli W. Tullis.

Data availability

Untargeted metabolomics data can be found at www.metabolomic-sworkbench.org, with project ID PR001193 or visit at https://doi.org/10.21228/M8H419. Untargeted metabolomics data were analyzed using the MetabolAnalyst v.5.0 platform (https://www.metaboanalyst.ca/). Source data are provided with this paper.

References

1. Swarup A et al. Modulating GLUT1 expression in retinal pigment epithelium decreases glucose levels in the retina: impact on photoreceptors and Müller glial cells. Am. J. Physiol. Cell Physiol 316, C121–C133 (2019). [PubMed: 30462537]
2. Kanow MA et al. Biochemical adaptations of the retina and retinal pigment epithelium support a metabolic ecosystem in the vertebrate eye. eLife 6, e28899 (2017). [PubMed: 28901286]
3. Winkler BS Glycolytic and oxidative metabolism in relation to retinal function. J. Gen. Physiol 77, 667–692 (1981). [PubMed: 6267165]
4. Punzo C, Kornacker K & Cepko CL Stimulation of the insulin/mTOR pathway delays cone death in a mouse model of retinitis pigmentosa. Nat. Neurosci 12, 44–52 (2009). [PubMed: 19060896]
5. Aït-Ali N et al. Rod-derived cone viability factor promotes cone survival by stimulating aerobic glycolysis. Cell 161, 817–832 (2015). [PubMed: 25957687]
6. Wang W et al. Two-step reactivation of dormant cones in retinitis pigmentosa. Cell Rep 15, 372–385 (2016). [PubMed: 27050517]
7. Young RW & Bok D Participation of the retinal pigment epithelium in the rod outer segment renewal process. J. Cell Biol 42, 392–403 (1969). [PubMed: 5792328]
8. Adijanto J et al. The retinal pigment epithelium utilizes fatty acids for ketogenesis: implications for metabolic coupling with the outer retina. J. Biol. Chem 289, 20570–20582 (2014). [PubMed: 24898254]
9. Wang W et al. Metabolic deregulation of the blood-outer retinal barrier in retinitis pigmentosa. Cell Rep 28, 1323–1334 (2019). [PubMed: 31365873]
10. Lynch SK & Abràmoff MD Diabetic retinopathy is a neurodegenerative disorder. Vis. Res 139, 101–107 (2017). [PubMed: 28408138]
11. Reiter CEN et al. Characterization of insulin signaling in rat retina in vivo and ex vivo. Am. J. Physiol. Endocrinol. Metab 285, E763–E774 (2003). [PubMed: 12799319]
12. James CR & Cotlier E Fate of insulin in the retina: an autoradiographic study. Br. J. Ophthalmol 67, 80–88 (1983). [PubMed: 6336953]
13. Zolov SN et al. Insulin-like growth factor-2 regulates basal retinal insulin receptor activity. J. Biol. Chem 10.1016/j.jbc.2021.100712 (2021).
14. Tarchick MJ et al. Endogenous insulin signaling in the RPE contributes to the maintenance of rod photoreceptor function in diabetes. Exp. Eye Res 180, 63–74 (2019). [PubMed: 30543793]
15. Rajala A, Tanito M, Le YZ, Kahn CR & Rajala RVS Loss of neuroprotective survival signal in mice lacking insulin receptor gene in rod photoreceptor cells. J. Biol. Chem 283, 19781–19792 (2008). [PubMed: 18480052]

16. Edwards RB & Szamier RB Defective phagocytosis of isolated rod outer segments by RCS rat retinal pigment epithelium in culture. Science 197, 1001–1003 (1977). [PubMed: 560718]
17. Burstyn-Cohen T et al. Genetic dissection of TAM receptor-ligand interaction in retinal pigment epithelial cell phagocytosis. Neuron 76, 1123–1132 (2012). [PubMed: 23259948]
18. Penberthy KK et al. Context-dependent compensation among phosphatidylserine-recognition receptors. Sci. Rep 7, 14623 (2017). [PubMed: 29116131]
19. Soares MB et al. RNA-mediated gene duplication: the rat preproinsulin I gene is a functional retroposon. Mol. Cell. Biol 5, 2090–2103 (1985). [PubMed: 2427930]
20. Anderson MS et al. Projection of an immunological self shadow within the thymus by the aire protein. Science 298, 1395–1401 (2002). [PubMed: 12376594]
21. Iacovelli J et al. Generation of Cre transgenic mice with postnatal RPE-specific ocular expression. Invest. Ophthalmol. Vis. Sci 52, 1378–1383 (2011). [PubMed: 21212186]
22. Van Cauter E, Mestrez F, Sturis J & Polonsky KS Estimation of insulin secretion rates from C-peptide levels. Comparison of individual and standard kinetic parameters for C-peptide clearance. Diabetes 41, 368–377 (1992). [PubMed: 1551497]
23. Wang S et al. Deciphering primate retinal aging at single-cell resolution. Protein Cell 10.1007/s13238-020-00791-x (2020).
24. Giddings SJ, Chirgwin J & Permutt MA The effects of fasting and feeding on preproinsulin messenger RNA in rats. J. Clin. Invest 67, 952–960 (1981). [PubMed: 6162861]
25. Boland BB et al. β-cell control of insulin production during starvation-refeeding in male rats. Endocrinology 159, 895–906 (2018). [PubMed: 29244064]
26. Unger RH, Eisentraut AM & Madison LL The effects of total starvation upon the levels of circulating glucagon and insulin in man. J. Clin. Invest 42, 1031–1039 (1963). [PubMed: 13995385]
27. Giddings SJ & Carnaghi LR The two nonallelic rat insulin mRNAs and pre-mRNAs are regulated coordinately in vivo. J. Biol. Chem 263, 3845–3849 (1988). [PubMed: 2831207]
28. Duvillié B et al. Phenotypic alterations in insulin-deficient mutant mice. Proc. Natl Acad. Sci. USA 94, 5137–5140 (1997). [PubMed: 9144203]
29. Leroux L et al. Compensatory responses in mice carrying a null mutation for Ins1 or Ins2. Diabetes 50, S150 (2001). [PubMed: 11272179]
30. Law A-L et al. Cleavage of Mer tyrosine kinase (MerTK) from the cell surface contributes to the regulation of retinal phagocytosis. J. Biol. Chem 290, 4941–4952 (2015). [PubMed: 25538233]
31. Rajala RVS & Anderson RE Light regulation of the insulin receptor in the retina. Mol. Neurobiol 28, 123–138 (2003). [PubMed: 14576451]
32. Sachdeva MM Retinal neurodegeneration in diabetes: an emerging concept in diabetic retinopathy. Curr. Diab. Rep 21, 65 (2021). [PubMed: 34902066]
33. Bok D & Hall MO The role of the pigment epithelium in the etiology of inherited retinal dystrophy in the rat. J. Cell Biol 49, 664–682 (1971). [PubMed: 5092207]
34. LaVail MM Rod outer segment disk shedding in rat retina: relationship to cyclic lighting. Science 194, 1071–1074 (1976). [PubMed: 982063]
35. Nandrot EF et al. Loss of synchronized retinal phagocytosis and age-related blindness in mice lacking αvβ5 integrin. J. Exp. Med 200, 1539–1545 (2004). [PubMed: 15596525]
36. Lu Q et al. Tyro-3 family receptors are essential regulators of mammalian spermatogenesis. Nature 398, 723–728 (1999). [PubMed: 10227296]
37. D'Cruz PM et al. Mutation of the receptor tyrosine kinase gene MerTK in the retinal dystrophic RCS rat. Hum. Mol. Genet 9, 645–651 (2000). [PubMed: 10699188]
38. Ryeom SW, Sparrow JR & Silverstein RL CD36 participates in the phagocytosis of rod outer segments by retinal pigment epithelium. J. Cell Sci 109, 387–395 (1996). [PubMed: 8838662]
39. Cai B et al. MerTK cleavage limits proresolving mediator biosynthesis and exacerbates tissue inflammation. Proc. Natl Acad. Sci. USA 113, 6526–6531 (2016). [PubMed: 27199481]
40. Villa E et al. mTORC1 stimulates cell growth through SAM synthesis and m6A mRNA-dependent control of protein synthesis. Mol. Cell 10.1016/j.molcel.2021.03.009 (2021).

41. Sinha T, Ikelle L, Naash MI & Al-Ubaidi MR The intersection of serine metabolism and cellular dysfunction in retinal degeneration. Cells 10.3390/cells9030674 (2020).
42. Ducker GS & Rabinowitz JD One-carbon metabolism in health and disease. Cell Metab 25, 27–42 (2017). [PubMed: 27641100]
43. Rajala A, Wang Y & Rajala RVS Activation of oncogenic tyrosine kinase signaling promotes insulin receptor-mediated cone photoreceptor survival. Oncotarget 7, 46924–46942 (2016). [PubMed: 27391439]
44. Venkatesh A et al. Activated mTORC1 promotes long-term cone survival in retinitis pigmentosa mice. J. Clin. Invest 125, 1446–1458 (2015). [PubMed: 25798619]
45. Akalu YT et al. Tissue-specific modifier alleles determine MerTK loss-of-function traits. eLife 11, e80530 (2022). [PubMed: 35969037]
46. Fan Y et al. Thymus-specific deletion of insulin induces autoimmune diabetes. EMBO J 28, 2812–2824 (2009). [PubMed: 19680229]
47. Li S et al. Rhodopsin-iCre transgenic mouse line for Cre-mediated rod-specific gene targeting. Genesis 41, 73–80 (2005). [PubMed: 15682388]
48. Xin-Zhao Wang C, Zhang K, Aredo B, Lu H & Ufret-Vincenty RL Novel method for the rapid isolation of RPE cells specifically for RNA extraction and analysis. Exp. Eye Res 102, 1–9 (2012). [PubMed: 22721721]
49. Fernandez-Godino R, Garland DL & Pierce EA Isolation, culture and characterization of primary mouse RPE cells. Nat. Protoc 11, 1206–1218 (2016). [PubMed: 27281648]
50. Venkatesh A, Ma S, Langellotto F, Gao G & Punzo C Retinal gene delivery by rAAV and DNA electroporation. Curr. Protoc. Microbiol 10.1002/9780471729259.mc14d04s28 (2013).
51. Wei H, Xun Z, Granado H, Wu A & Handa JT An easy, rapid method to isolate RPE cell protein from the mouse eye. Exp. Eye Res 145, 450–455 (2016). [PubMed: 26424220]
52. Sheybani ND et al. ImmunoPET-informed sequence for focused ultrasound-targeted mCD47 blockade controls glioma. J. Control. Release 331, 19–29 (2021). [PubMed: 33476735]
53. Zhong M & Kundu BK Optimization of a model corrected blood input function from dynamic FDG-PET images of small animal heart in vivo. IEEE Trans. Nucl. Sci 60, 3417–3422 (2013). [PubMed: 24741130]
54. Huang Q, Massey JC, Mińczuk K, Li J & Kundu BK Non-invasive determination of blood input function to compute rate of myocardial glucose uptake from dynamic FDG PET images of rat heart in vivo: comparative study between the inferior vena cava and the left ventricular blood pool with spill over and partial volume corrections. Phys. Med. Biol 64, 165010 (2019). [PubMed: 31307015]
55. Tsugawa H et al. MS-DIAL: data-independent MS/MS deconvolution for comprehensive metabolome analysis. Nat. Methods 12, 523–526 (2015). [PubMed: 25938372]
56. Tsugawa H et al. A cheminformatics approach to characterize metabolomes in stable-isotope-labeled organisms. Nat. Methods 16, 295–298 (2019). [PubMed: 30923379]
57. Narendran S et al. Nucleoside reverse transcriptase inhibitors and Kamuvudines inhibit myloid-β induced retinal pigmented epithelium degeneration. Signal Transduct. Target Ther 6, 1–9 (2021). [PubMed: 33384407]

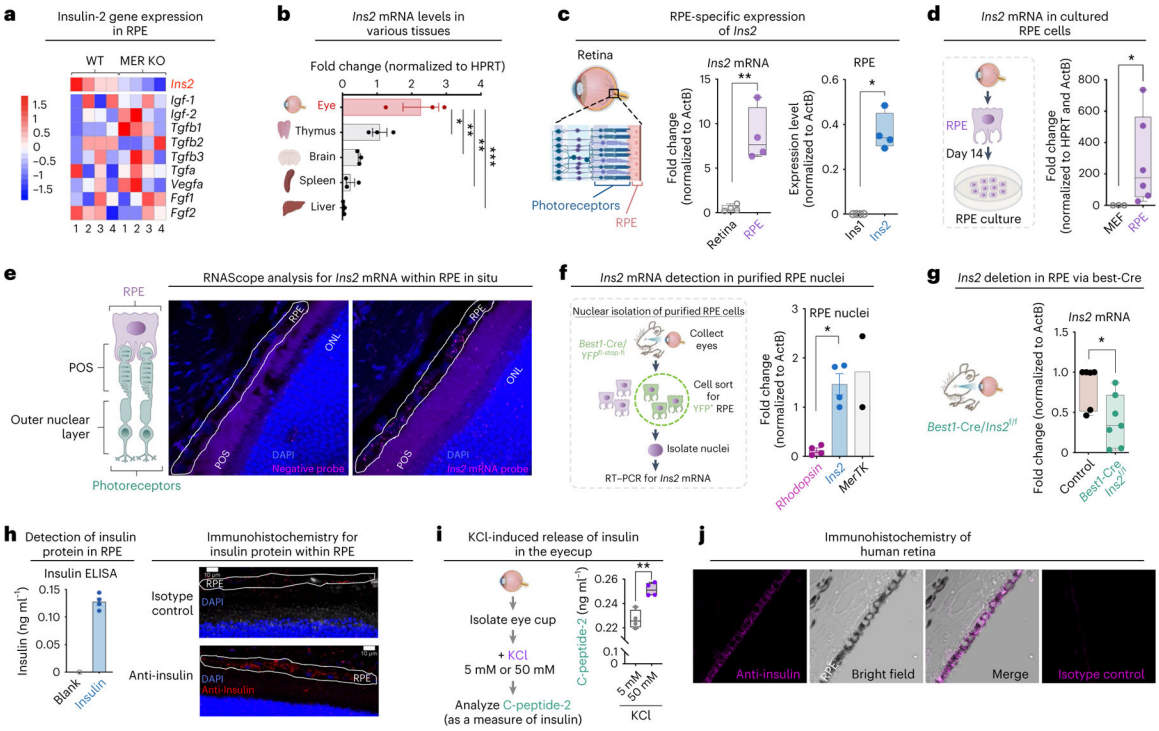

Fig. 1 |. Expression of *Ins2* mRNA and protein within the RPE.

a, *Ins2* detection in RNA-seq of RPE from WT and *MerTK* KO mice. While *Ins2* was lower in *MerTK* KO mice, other growth factors were unaltered (false discovery rate (FDR) ≤ 0.5). Scale corresponds to z score. $n = 4$ mice per genotype. **b**, *Ins2* expression in different tissues by RT–PCR. $n = 3$ mice per tissue. HPRT, hypoxanthine-guanine phosphoribosyl transferase. **c**, RT–PCR comparing *Ins2* expression in retina versus RPE (middle) and *Ins1* versus *Ins2* in RPE (right). $n = 4$ mice. **d**, *Ins2* mRNA in primary cultured RPE cells ($n = 6$ mice) and control mouse embryonic fibroblasts ($n = 3$). **e**, Schematic of RPE and photoreceptors (left). Representative image of three independent experiments showing *Ins2* transcript (magenta) within RPE of mouse retina via confocal microscopy using RNAScope Multiplex-Fluorescent assay at ×60 magnification (right). A scrambled 'nonsense' negative probe was used as control. **f**, Isolated nuclei of RPE contain *Ins2* mRNA. Schematic of RPE purification and nuclei isolation from *Best1*-Cre/YFP$^{\text{flox-STOP-flox}}$ mice (left). Analysis of indicated genes by RT–PCR (right). $n = 4$ mice used for *rhodopsin* and *Ins2*, $n = 2$ mice for *MerTK*. **g**, *Ins2* expression in RPE from *Best1*-Cre Ins$^{2f/f}$ mice. $n = 6$ mice control, $n = 7$ *Best1*-Cre Ins$^{2f/f}$. **h**, ELISA of insulin in protein lysates of RPE. $n = 4$ mice (left). Representative image of three independent experiments showing immunofluorescence on mouse retina using anti-insulin or isotype-control antibody (red) and DAPI for cell nuclei (right). RPE is outlined in white. **i**, Isolated eye cups (RPE/choroid/sclera) of WT mice were treated with KCl and supernatants were analyzed for C-peptide-2 by ELISA. **j**, Representative immunofluorescence image of human retina stained with anti-insulin (magenta) with brightfield microscopy showing RPE (appearing black due to pigment granules). Isotype antibody was used as control. Bar graphs are mean ± s.e.m. Box and whiskers show minimum to maximum values, center denotes median and the bounds denote the 25th to 75th percentiles. $*P \leq 0.05$,$**P \leq 0.01$,$***P \leq 0.001$, one-way analysis of

variance (ANOVA) with Tukey's multiple comparisons test (**b**), unpaired two-tailed *t*-test (**c**,**g**–**i**) and nonparametric Mann–Whitney *U*-test (**d**,**f**).

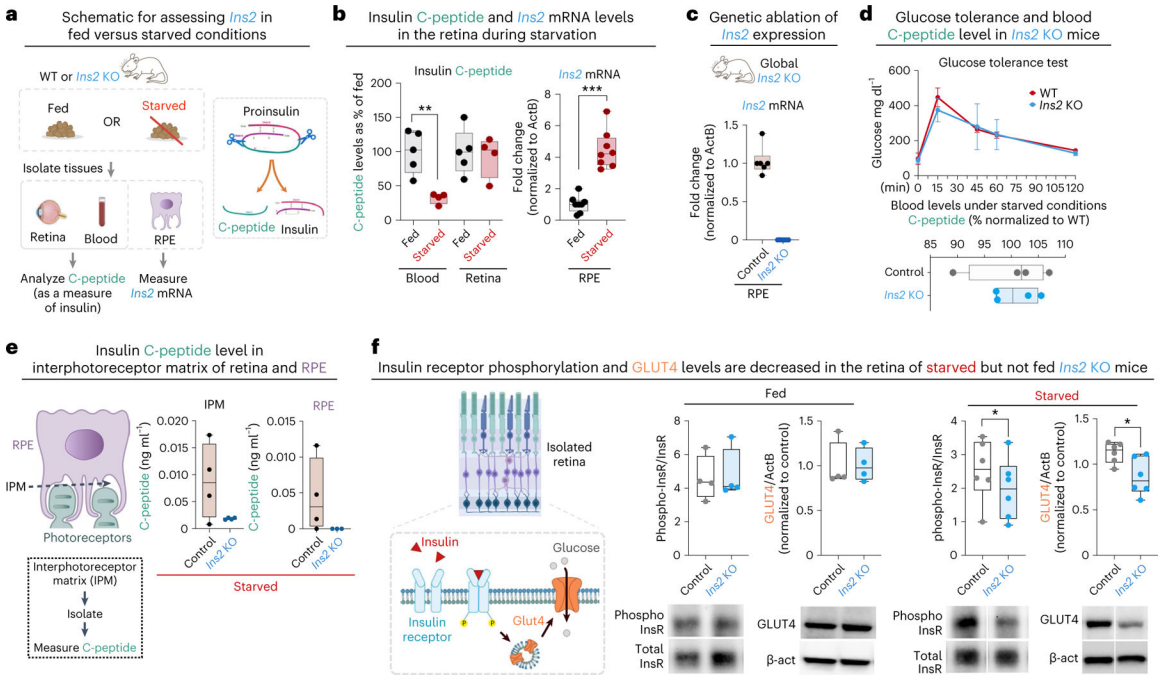

Fig. 2 |. *Ins2* expression in the RPE is regulated differently from systemic insulin.

a, Schematic for measuring C-peptide and *Ins2* mRNA in fed and starved (10–14 h) conditions (left) and C-peptide cleavage during insulin synthesis (right). **b**, ELISA for C-peptide in blood and protein lysates from retina of fed (ad libitum) and starved mice. Y axis shows percentage of C-peptide found in fed mice. $n = 5$ mice for fed condition, $n = 4$ mice for starved. RT–PCR comparing *Ins2* expression in RPE from fed or starved mice (right). $n = 8$ mice per condition. **c**, RT–PCR measuring *Ins2* in RPE from control and *Ins2* KO mice. $n = 6$ mice per genotype. **d**, Glucose tolerance assay (readout of insulin function) measuring circulating glucose levels over time in WT and *Ins2* KO mice starved and then given glucose intraperitoneally (top). $n = 4$ mice per genotype. ELISA for C-peptide in blood of control and *Ins2* KO mice shows no difference between genotypes (bottom). $n = 4$ mice per genotype. **e**, Schematic of the IPM (left). IPM was isolated from WT and *Ins2* KO mice and the secreted C-peptide in IPM was measured by ELISA (middle). $n = 4$ mice per genotype. ELISA of C-peptide in lysates of RPE from WT and *Ins2* KO mice (right). $n = 4$ mice WT, $n = 3$ *Ins2* KO. **f**, Insulin receptor was immunoprecipitated from retina lysates of control and *Ins2* KO mice, either fed or starved. InsR tyrosine phosphorylation was assessed using phospho-specific InsR antibodies via immunoblotting and quantified as the ratio of p-InsR to total InsR. Retina lysates were also probed for GLUT4 and quantified as the ratio of GLUT4 to actin (normalized to control). $n = 4$ mice for fed, $n = 6$ starved conditions. Plots are presented as in Fig. 1. $*P \leq 0.05$,$**P \leq 0.01$,$***P \leq 0.001$, unpaired two-tailed *t*-test (**b**) and paired two-tailed *t*-test (**f**).

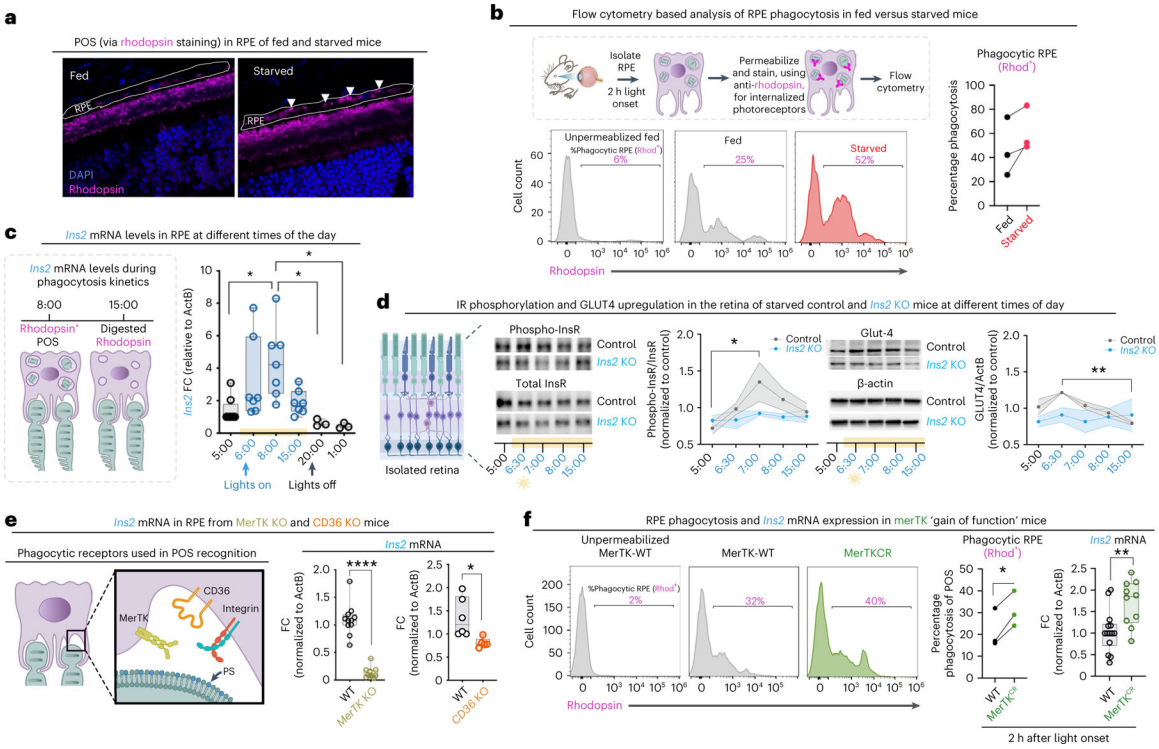

Fig. 3 |. Phagocytosis upregulates *Ins2* expression in the RPE.

a, Representative image of three independent experiments showing immunofluorescence analysis with anti-rhodopsin (magenta) on retina sections 2 h after light onset (peak phagocytosis time) from fed and starved (10–14 h) mice. Sections were counterstained with 4,6-diamidino-2-phenylindole (DAPI) (blue). RPE is outlined in white. **b**, Flow cytometry-based phagocytosis assay on isolated fixed and permeabilized RPE stained with rhodopsin, from fed or starved mice, obtained 2 h after light onset. Phagocytosis was measured as % of rhodopsin$^+$ RPE within total RPE. $n = 3$ mice per condition. **c**, RT–PCR for *Ins2* expression in RPE from fed mice at different times of the day. Lights on at 6:00 and lights off at 20:00. $n = 8$, 7, 7, 7, 3 and 3 mice used for times of 5:00, 6:00, 8:00, 15:00, 20:00 and 1:00, respectively. FC, fold change. **d**, InsR immunoprecipitated from retina lysates, at different times of day from overnight starved control and *Ins2* KO mice, were probed using phospho-specific InsR antibodies. The same retina lysates were probed for GLUT4. Values were normalized to the average of control across all time points. $n = 3$ mice for each time point. **e**, Schematic of phagocytic receptors used in POS recognition (left). RT–PCR for *Ins2* in RPE isolated from WT and *MerTK* KO or *CD36* KO mice 2 h after light onset (right). $n = 10$ and 11 mice for WT versus *MerTK* KO and $n = 6$ and 5 mice for WT versus *CD36* KO. **f**, Phagocytosis quantification using flow cytometry on isolated RPE from WT and MerTK^{CR} mice (middle). $n = 3$ mice used per genotype. RT–PCR measuring *Ins2* expression in isolated RPE from WT and MerTK^{CR} (right). $n = 14$ and 10 mice for WT and MerTK^{CR}, respectively. Plots are presented as in Fig. 1. $*P \leq 0.05$,$**P \leq 0.01$,$***P \leq 0.001$, $****P \leq 0.0001$, one-way ANOVA (**c**), two-way ANOVA with Tukey's multiple comparisons test (**d**), unpaired two-tailed *t*-test (**e**,**f** RT–PCR) and paired two-tailed *t*-test (**f** phagocytosis quantification).

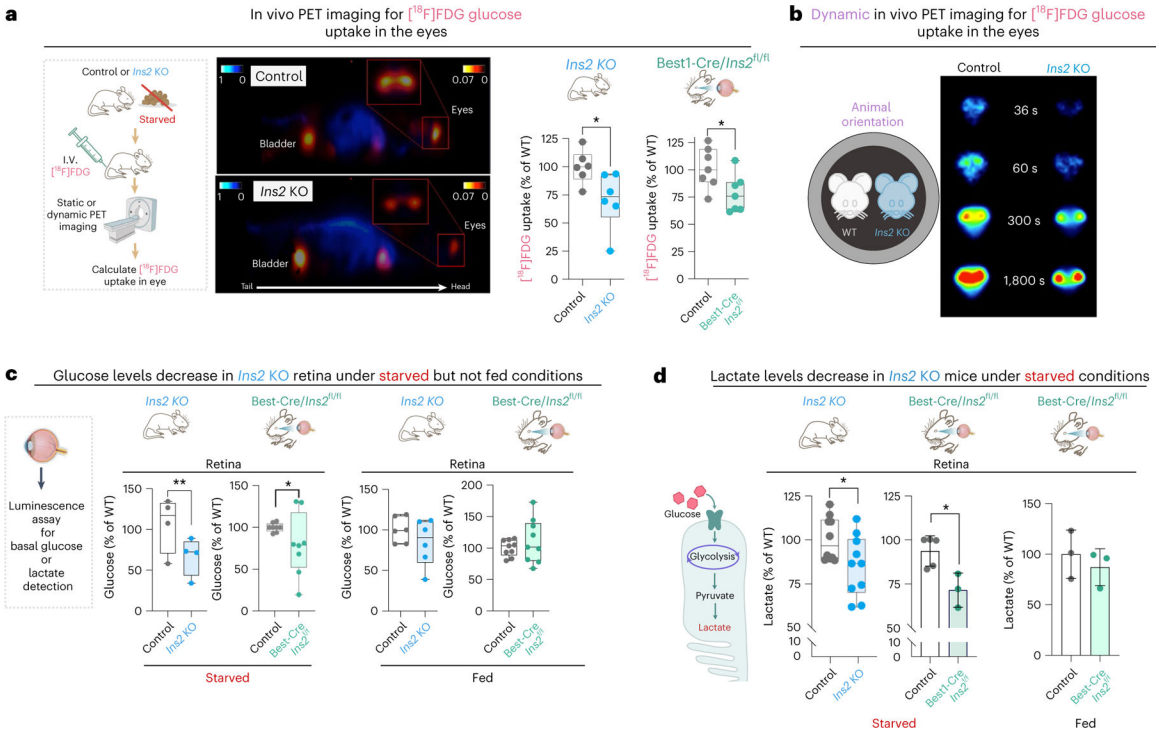

Fig. 4 |. Loss of *Ins2* decreases glucose uptake and alters retinal homeostasis.

a, Schematic of PET imaging (left). Parametric [^{18}F]FDG glucose PET Ki uptake map in the eye of control and *Ins2* KO mice (middle). Red intensity indicates glucose uptake in tissue and blue intensity indicates glucose levels in blood. Boxes outline eyes and inset represents a coronal view of eyes from uptake map. Quantification of glucose uptake in eyes of control and *Ins2* KO or *Best1*-Cre Ins$^{2f/f}$ mice using static PET imaging (right). Values on the *y* axis are % glucose uptake relative to control. $n = 6$ mice control and *Ins2* KO, $n = 7$ mice control and *Best1*-Cre Ins$^{2f/f}$. $^{*}P \leq 0.05$, unpaired *t*-test. **b**, Snap shots of dynamic in vivo PET imaging for [^{18}F]FDG glucose uptake in the eye at 36, 60, 300 and 1,800 seconds after [^{18}F]FDG injection. Red intensity indicates glucose uptake. **c**, Quantification of glucose levels in isolated retina of fed or starved control, *Ins2* KO or *Best1-Cre Ins$^{2f/f}$* mice using luciferase glucose detection assay. Values on the y axis are presented as % of glucose relative to control. $n = 4$ starved control and *Ins2* KO mice, $n = 8$ starved control and *Best1-Cre Ins$^{2f/f}$* mice, $n = 6$ fed control and *Ins2* KO and $n = 9$ fed control and *Best1-Cre Ins$^{2f/f}$* mice. $^{*}P \leq 0.05$ permutation test, $^{**}P \leq 0.01$ unpaired *t*-test. **d**, Schematic of lactate generation in photoreceptors (left). Quantification of lactate in isolated retina of fed or starved control mice, *Ins2* KO or *Best1-Cre Ins$^{2f/f}$* mice, using luciferase lactate detection assay. Values on the y axis are % lactate relative to control. $n = 10$ mice used for starved control and *Ins2* KO, $n = 4$ and 3 mice for starved control and *Best1-Cre Ins$^{2f/f}$* and $n = 3$ mice fed control and *Best1-Cre Ins$^{2f/f}$*. $^{*}P \leq 0.05$ unpaired *t*-test for *Ins2* KO, $^{*}P \leq 0.05$ nonparametric Mann–Whitney *U*-test for *Best1-Cre Ins$^{2f/f}$*. Plots are presented as in Fig. 1.

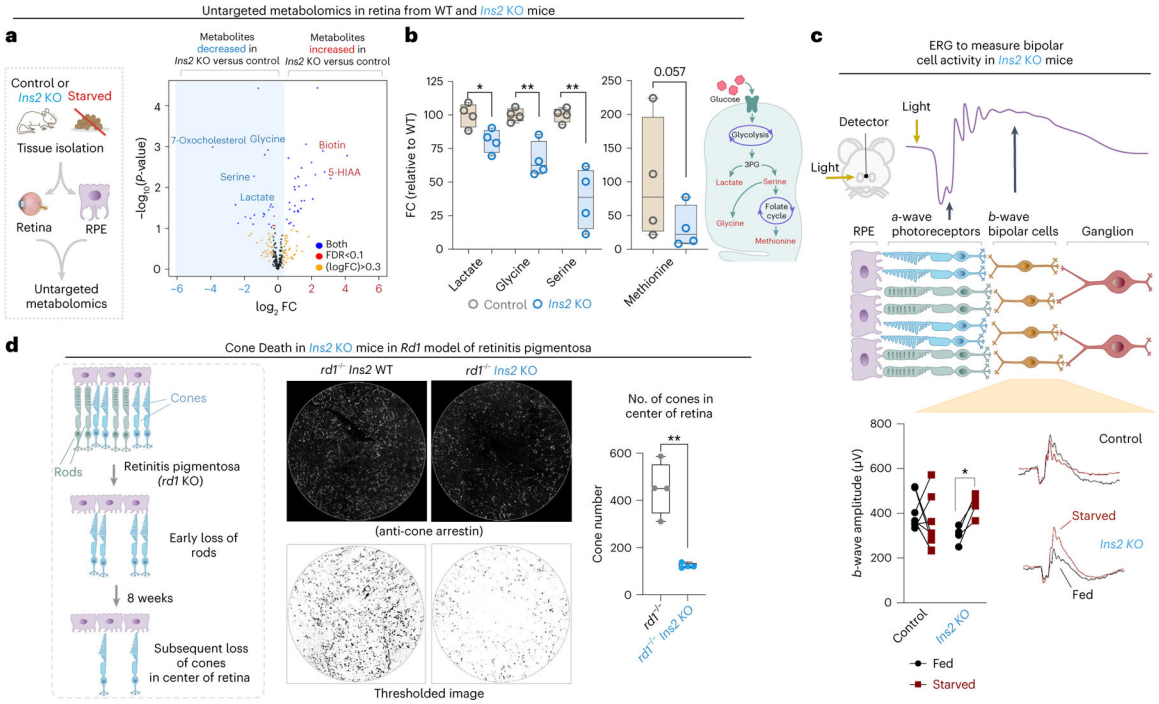

Fig. 5 |. *Ins2* regulates retinal metabolic homeostasis and retinal disease.

a, Schematic of untargeted metabolomics of retinas and RPE from starved WT and *Ins2* KO mice (left). Volcano plot from untargeted metabolomics of retinas representing statistically enriched or reduced metabolites in retinas of control mice relative to those of *Ins2* KO (right) using Fisher's exact test. FDR $P < 0.1$ in red, absolute value of the $\log_2$ fold change (FC) of 0.3 (1.2 fold change) in orange and blue meets both criteria. Data are representative of four biological replicates. **b**, Schematic of select glucose-dependent metabolic pathways in photoreceptors (right). Aerobic glycolysis in photoreceptors leads to the production of lactate from glucose. Glucose in photoreceptors can be converted to serine, which is crucial for glycine production and the folate methionine cycle. Metabolomic analysis reveals that these metabolites are decreased in *Ins2* KO retinas compared to WT (left). $*P < 0.05$, $**P < 0.01$ two-sided Wald two-sample *t*-test. Data are representative of four biological replicates. **c**, Schematic of scotopic ERG on mouse retina to detect visual processing in response to light (top). Quantification of b-wave amplitude in ERG of WT and *Ins2* KO mice under fed and starved condition (bottom). Representative ERG traces for control and *Ins2* KO (bottom right) $n = 8$ mice for WT, $n = 4$ mice for *Ins2* KO mice. $*P \leq 0.05$ two-way ANOVA with Fisher's LSD test. **d**, Schematic of the rd1 mouse model of retinitis pigmentosa (left). Representative image of immunofluorescence on the center retina of 8-week-old rd1 and *Ins2* KO.rd1 mice using antibodies against arrestin in cone cells (top). Thresholding of immunofluorescence images (bottom), where pixels above a certain value are replaced with a black pixel. Quantification of the number of cones located in the center retina of rd1 and *Ins2* KO.rd1 mice (right). $n = 4$ mice for both genotypes. $*P \leq 0.05$ unpaired *t*-test. Plots are presented as in Fig. 1.